Low-Level Z_{DR} Signatures in Supercell Forward Flanks: The Role of Size Sorting and Melting of Hail

DANIEL T. DAWSON II,*,+ EDWARD R. MANSELL,# YOUNGSUN JUNG,@ LOUIS J. WICKER,# MATTHEW R. KUMJIAN,& AND MING XUE@

* *NOAA/National Severe Storms Laboratory, and Cooperative Institute for Mesoscale Meteorological Studies, Norman, Oklahoma*
# *NOAA/National Severe Storms Laboratory, Norman, Oklahoma*
@ *Center for Analysis and Prediction of Storms, University of Oklahoma, Norman Oklahoma*
& *National Center for Atmospheric Research, Boulder, Colorado*

(Manuscript received 20 April 2013, in final form 12 July 2013)

ABSTRACT

The low levels of supercell forward flanks commonly exhibit distinct differential reflectivity (Z_{DR}) signatures, including the low-Z_{DR} hail signature and the high-Z_{DR} "arc." The Z_{DR} arc has been previously associated with size sorting of raindrops in the presence of vertical wind shear; here this model is extended to include size sorting of hail. Idealized simulations of a supercell storm observed by the Norman, Oklahoma (KOUN), polarimetric radar on 1 June 2008 are performed using a multimoment bulk microphysics scheme, in which size sorting is allowed or disallowed for hydrometeor species. Several velocity–diameter relationships for the hail fall speed are considered, as well as fixed or variable bulk densities that span the graupel-to-hail spectrum. A T-matrix-based emulator is used to derive polarimetric fields from the hydrometeor state variables.

Size sorting of hail is found to have a dominant impact on Z_{DR} and can result in a Z_{DR} arc from melting hail even when size sorting is disallowed in the rain field. The low-Z_{DR} hail core only appears when size sorting is allowed for hail. The mean storm-relative wind in a deep layer is found to align closely with the gradient in mean mass diameter of both rain and hail, with a slight shift toward the storm-relative mean wind below the melting level in the case of rain. The best comparison with the observed 1 June 2008 supercell is obtained when both rain and hail are allowed to sort, and the bulk density and associated fall-speed curve for hail are predicted by the model microphysics.

1. Introduction

Dual-polarized radars have many advantages over their single-polarized counterparts, particularly an enhanced ability to distinguish between different types, sizes, and shapes of hydrometeors within precipitating systems (e.g., Balakrishnan and Zrnić 1990; Herzegh and Jameson 1992; Ryzhkov and Zrnić 1998; Zrnić and Ryzhkov 1999; Straka et al. 2000; Bringi and Chandrasekar 2001; Zrnić et al. 2001; Ryzhkov et al. 2005a; Tessendorf et al. 2005; Heinselman and Ryzhkov 2006; Park et al. 2009), and to distinguish between hydrometeors and other nonmeteorological scatterers, such as insects, birds, dust, and debris (e.g., Ryzhkov et al. 2005b; Gourley et al. 2007). Several polarimetric variables can be derived from the information provided by the horizontally and vertically polarized beams and their differential interactions with hydrometeors.[1] Among these, the differential reflectivity Z_{DR} (the ratio of radar reflectivity factors at horizontal and vertical polarizations; Seliga and Bringi 1976) is useful for distinguishing between regions of hail and rain. Further, it is substantially positive (depending

+ Current affiliation: Center for Analysis and Prediction of Storms, University of Oklahoma, Norman, Oklahoma.

Corresponding author address: Daniel T. Dawson II, Center for Analysis and Prediction of Storms, University of Oklahoma, 120 David L. Boren Blvd., Norman, OK 73072.
E-mail: ddawson@ou.edu

[1] The polarimetric Weather Surveillance Radar-1988 Doppler (WSR-88D) operates using a mode of simultaneous transmission of horizontally and vertically polarized waves, resulting in slant-45 polarization.

DOI: 10.1175/JAS-D-13-0118.1

on the radar wavelength) for rain distributions skewed toward large oblate drops. In combination with other polarimetric variables, Z_{DR} yields much information about the particle size distribution [PSD; or drop size distribution (DSD)] of rain, which aids in improving radar-derived rain-rate relations (e.g., Bringi et al. 2004; Giangrande and Ryzhkov 2008) and understanding of microphysical processes and their relationship to the kinematics of storms, which is the subject of the present study.

Among precipitating cloud systems, supercell thunderstorms produce some of the most severe localized weather on the planet, including large hail, damaging straight-line winds, and tornadoes. Recent studies have shown that supercells systematically display certain (possibly unique) polarimetric signatures, which have yielded significant insight into the complex interplay of kinematics and microphysical processes within these storms (Kumjian and Ryzhkov 2008; Romine et al. 2008; Jung et al. 2010, hereafter JXZ10). One of the most common polarimetric signatures noted is the Z_{DR} ''shield'' or ''arc.''[2] This signature appears within the forward-flank reflectivity region at low levels (below about 1–2 km AGL) and is characterized by significant positive values of Z_{DR} collocated with low-to-moderate reflectivity. Kumjian and Ryzhkov (2009, 2012, hereafter KR09 and KR12, respectively), used a simplified bin sedimentation model to interpret the Z_{DR} arc as a result of enhanced size sorting of rain associated with the strong low-level shear in the inflow environment of the supercell storm, and also demonstrated a positive correlation with the magnitude of the low-level storm-relative helicity and the ''strength'' of the Z_{DR} arc.

KR09 and KR12 limited their investigation to idealized rain shafts with prescribed initial distributions aloft. In typical supercell storms, most of the rain is derived from the melting of ice particles, particularly snow, graupel, and hail. Romine et al. (2008), in their study of the 8 May 2003 Oklahoma City, Oklahoma, tornadic supercell, attributed the source of large drops in the Z_{DR} shield as melted graupel. Kumjian et al. (2010, hereafter KRMS10) also explicitly identify the source of rain in the Z_{DR} arc as melted graupel in their study of the 1 June 2008 western Oklahoma nontornadic supercell. Below the melting level, a given area of the precipitation region may include contributions to Z_{DR} from both rain and partially melted graupel or hail. The Z_{DR} signature of the latter can vary significantly depending on the size of the hydrometeors and the amount of water coating. For relatively dry, large, and tumbling hailstones, the Z_{DR} is near 0 dB. At the other end of the spectrum, small, nearly completely melted hailstones transition to a maximum stable large raindrop (Rasmussen et al. 1984, hereafter RLP84), and thus exhibit high Z_{DR}. It remains an open question how much of the low-level (~0–2 km) enhanced Z_{DR} in the forward flanks of supercells can be attributed to melting graupel or hail versus rain. Other polarimetric variables, such as the cross-correlation coefficient ρ_{HV} and specific differential phase K_{DP}, are also helpful in this regard: the former is sensitive to mixtures of rain and hail and the latter to the presence of liquid water, whether in raindrops or as a shell of liquid water on melting graupel and hail.

A major challenge in numerical modeling of convective storms is the treatment of the rimed-ice category or categories (graupel or hail or both), particularly assumptions about the bulk density and fall speeds (e.g., Gilmore et al. 2004). The sorting of the graupel and hail fields in the presence of environmental shear above the melting level has been relatively unexplored, particularly how it then contributes to shaping the distribution of rain and melting graupel and hail sizes below the melting level, which can modify the observed Z_{DR} there in complex ways. The depth of the shear layer in supercell environments often extends well above the melting level [O(3–5 km)], and thus substantial sorting of graupel and hail may occur long before melting occurs. Motivated by these questions, we investigate the impact of size sorting and melting on the magnitudes of Z_{DR} below the melting level through the use of numerical simulation. Our first approach is to examine 3D idealized numerical simulations of a well-observed supercell: the 1 June 2008 nontornadic supercell that was the subject of KRMS10. We show how the basic polarimetric features (with an emphasis on the Z_{DR} field) in the low levels of the forward flank can be reasonably reproduced by a triple-moment (3M) bulk microphysics scheme, particularly when the bulk density of the rimed-ice category is predicted, rather than held fixed as is usually the case. Then, to simplify the analysis and in an attempt to reveal the essential physics, we make use of relatively simple environmental setups that are reminiscent of the steady 3D precipitation-shaft experiments of KR09, but instead inject graupel/hail above the melting level, which then falls and melts into rain. In both sets of experiments, similar to KR12, we investigate the impact of size sorting by differential sedimentation and demonstrate the separate impacts of sorting of graupel and hail on the one hand, and rain on the other, on the low-level Z_{DR} signatures.

[2] Whether the Z_{DR} arc and shield is the same feature remains an open question. While this work does not address this question directly, we find it plausible that the Z_{DR} arc may be a small-scale enhancement of the Z_{DR} shield that may not be explicitly resolved with the resolution of the models used in this study. Future work may address this question.

This paper is organized as follows. Section 2 describes aspects of the bulk microphysics scheme and the polarimetric emulator used to derive Z_{DR} from the model microphysics fields. Sections 3 and 4 describe the methodology and results of the supercell simulation experiments and 3D precipitation shaft experiments, respectively. Finally, section 5 summarizes the paper and discusses questions to guide future work.

2. Microphysics scheme and polarimetric emulator

a. Microphysics scheme

The microphysics scheme used in this study is an upgraded version of the multimoment (MM) scheme described in Mansell et al. (2010, hereafter MZB10), developed at the National Severe Storms Laboratory (NSSL), which itself is based on an earlier scheme of Ziegler (1985). The full scheme allows for multiple options at runtime to control various microphysical processes and levels of complexity, such as the number of moments predicted, whether only one rimed-ice category (generically named graupel/hail, but can also be characterized as graupel, frozen drops, or small hail, depending on size, density, and fall-speed assumptions) or two (graupel/hail and large hail) are included, and whether the bulk densities of graupel/hail and large hail are allowed to vary (Mansell and Ziegler 2013), among others. Note that the graupel/hail category with predicted density can emulate a range of particle types, from low-density graupel to small frozen drops to small hail, and may be referred to as either graupel or hail, depending on the dominant characteristic. The large-hail category simulates hail converted from larger, high-density graupel/hail during wet growth and will be referred to specifically as ''large hail.'' Up to three moments of the gamma size distribution are predicted for graupel/hail, large hail, and rain—the zeroth, third, and sixth moments—following the approach of Milbrandt and Yau (2005a,b, hereafter MY05a,b), but only the first two moments for the remaining species. The closure scheme for the sixth-moment rate equations mainly follows the approach of MY05b (see the appendix), and the reader is otherwise referred to MZB10 for a description of the microphysics scheme. In the current study, we utilize only one rimed-ice category (i.e., large hail is deactivated) in all but one of the experiments. However, since the variation of the fall speeds with density can be substantial, we investigate the impact of maintaining fixed bulk densities for rimed ice of $500\,\mathrm{kg\,m^{-3}}$ (graupel like) and $900\,\mathrm{kg\,m^{-3}}$ (hail like) on the one hand, and allowing the rimed-ice category to vary in density (a spectrum of graupel to hail), as in MZB10, on the other. For convenience, throughout the paper, when using fixed bulk densities for graupel/hail, the term ''graupel'' will be used for the medium-density ($500\,\mathrm{kg\,m^{-3}}$) slower-falling case, while the term ''hail'' will be used for the high-density ($900\,\mathrm{kg\,m^{-3}}$) faster-falling case. In the variable-density experiments, the term ''hail'' will be used, mainly because, as will be discussed, the density and fall speeds have already risen to the ''hail like'' part of the spectrum by the time the hydrometeors have fallen much below the melting level owing to the increase in density during melting. These configurations of the scheme will be referred to as the NSSL fixed density (NFD) and NSSL variable density (NVD) schemes [after Yussouf et al. (2013)].

A quantity that will be used throughout this paper is the mean mass (or mean volume) diameter D_m, which is defined as

$$D_{mx} = \left(\frac{6\rho_a q_x}{\pi \rho_x N_{Tx}}\right)^{1/3}, \tag{1}$$

where ρ_a is the air density, q_x is the mass mixing ratio, ρ_x is the bulk hydrometeor density, and N_{Tx} is the total number concentration. The subscript x refers to any given hydrometeor category: r is rain, h is hail, and g is graupel. This form of D_m is valid for constant density spheres. As described in MY05a, this quantity serves as a proxy for the amount of size sorting that has occurred in the hydrometeor distribution, when compared to its initial value aloft. Physically speaking, D_m represents the diameter of the particle whose mass is equal to that of the mean mass of the distribution.

The terminal velocities of graupel and hail are assumed to follow a power law with respect to diameter of the form $v(D) = \gamma a D^b$, where a and b are typically empirically derived constants, and $\gamma = (\rho_0/\rho_a)^{0.5}$ is the density correction factor, where $\rho_0 = 1.204\,\mathrm{kg\,m^{-3}}$ and ρ_a is the air density. The power-law relationships used in this study are summarized in Fig. 1 and Table 1. The labels A–D in Fig. 1 are used in the experiment naming nomenclature to be discussed later in the paper. Curves A and B are derived from the terminal velocity relation for graupel and hail as used in Wisner et al. (1972) and adopted by MZB10. They depend on the assumed hydrometeor bulk density and drag coefficient, with increasing terminal fall speeds for all diameters as the bulk density increases. Thus, curve A represents graupel with a fixed density of $500\,\mathrm{kg\,m^{-3}}$ and likewise curve B for hail ($900\,\mathrm{kg\,m^{-3}}$). Curves C and D are from Ferrier (1994) for graupel and hail, respectively. When graupel and hail are allowed to vary in density, the resulting fall-speed curves lie between the lowest-density ($170\,\mathrm{kg\,m^{-3}}$) curve and the high-density ($900\,\mathrm{kg\,m^{-3}}$) curve (bottom

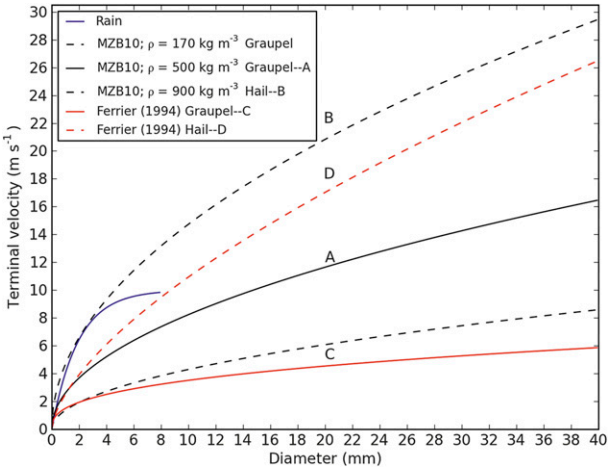

FIG. 1. Terminal velocity–diameter relations for rain, graupel, and hail, as used in the NFD and NVD schemes. The letter labels are used in the experiment names to indicate which fall-speed relation for graupel or hail is assumed for the NFD experiments. For the NVD experiments, the graupel/hail density is allowed to vary between the two curves given by the black dashed lines.

and top black dashed lines in Fig. 1, respectively). This variability in the assumed fall-speed relations has consequences for the distribution of graupel and hail [also noted explicitly by Milbrandt and Morrison (2013)] and on the distribution of Z_{DR} in the simulations in this study.

Several recent studies (Wacker and Seifert 2001; MY05a; Dawson et al. 2010; Mansell 2010; Milbrandt and McTaggart-Cowan 2010; KR12) have demonstrated the following characteristics of typical bulk microphysics schemes in regard to the size-sorting process: 1) single-moment (1M) schemes are incapable of parameterizing size sorting, 2) double-moment (2M) schemes without a correction mechanism (e.g., Mansell 2010) or diagnostic formula for the gamma shape parameter (MY05a; Milbrandt and McTaggart-Cowan 2010) can grossly overestimate size sorting of faster-falling hydrometeors, and 3) 3M schemes are able to closely approximate an analytical bin solution for pure sedimentation. The lack of size sorting in a 1M scheme is a consequence of the use of a single predicted variable (q, the total mass), from which all other PSD-related variables (including D_m) are diagnosed. In contrast, the size-sorting mechanism in a MM bulk scheme works by allowing each predicted moment of the size distribution to sediment at its own moment-weighted fall speed (Srivastava 1978), such that number concentration can evolve independently of total mass. For a 2M scheme that predicts N_T and q, the mass-weighted fall speed is greater than the number-weighted fall speed, allowing more q to reach lower levels faster than N_T, increasing D_m toward the ground (MY05a). Similarly, in a 3M scheme that predicts N_T, q, and Z, the reflectivity-weighted fall speed is generally greater than the mass-weighted fall speed, resulting in an increase of the shape parameter [α in (A1)] in the gamma distribution during size sorting. A larger shape parameter narrows the size distribution and limits further size sorting by causing the weighted fall speeds to be closer in value. A 2M scheme does not have this feedback and can exhibit unrealistically large D_m during the size-sorting process unless mitigating steps are taken (e.g., MY05a; Mansell 2010).

JXZ10 showed that a 2M scheme was at least qualitatively able to reproduce many of the common supercell polarimetric signatures. Based on the above-mentioned arguments, however, in the context of MM bulk schemes a 3M scheme is the most appropriate for studying polarimetric radar signatures that depend on size-sorting effects. For this reason, we utilize the 3M version of the NFD and NVD schemes for the experiments in this study, but we alternately enable or disable size sorting by either allowing all predicted moments to sediment at their appropriately weighted fall speed (the "3M" experiments) or by forcing all three predicted moments to instead sediment at the mass-weighted fall speed, effectively making the process of sedimentation only 1M for these experiments (called the "1M" experiments). We emphasize, however, that in all experiments all other processes are still fully 3M, and all three moments are tracked independently in the model.

TABLE 1. Summary of fall-speed relations for rain, graupel, and hail.

Category	Fall-speed relation	a_x	b_x
Rain	$v_{tr} = \gamma a_r[1 - \exp(-b_r D)]$	10	516.575
Graupel—A	$v_{tg} = \gamma a_g D^{b_g}$	$a_g = \dfrac{4\rho_g g}{3C_D\rho_a}$, $C_D = 0.8$	0.5
Hail—B	$v_{th} = \gamma a_h D^{b_h}$	$a_h = \dfrac{4\rho_h g}{3C_D\rho_a}$, $C_D = 0.45$	0.5
Graupel—C	$v_{tg} = \gamma a_g D^{b_g}$	19.3	0.37
Hail—D	$v_{th} = \gamma a_h D^{b_h}$	206.984	0.6384
Variable density graupel/hail	$v_{tg/h} = \gamma a_{g/h} D^{b_{g/h}}$	$a_{g/h} = \dfrac{4\rho_h g}{3C_D\rho_a}$, $C_D = 0.45$–1.0, $\rho_{g/h} = 170$–$900\,\mathrm{kg\,m^{-3}}$	0.5

b. Polarimetric emulator

To derive polarimetric fields from the model hydrometeor fields, we employ a modified version of the polarimetric emulator of JXZ10. In what follows, we stress that the emulator is applied to the model hydrometeor fields entirely ''offline''—that is, no feedback from the emulator is provided to the model; it is an entirely diagnostic procedure. The JXZ10 emulator uses the T-matrix method (Waterman 1969; Vivekanandan et al. 1991; Mishchenko 2000) to create scattering-amplitude lookup tables for all hydrometeor categories as a function of particle diameter and assumed liquid water fraction in the case of the ice categories. The emulator can accommodate radar wavelengths at X, C, and S bands, but we examine only the S-band case in this study for comparison with the S-band Norman, Oklahoma (KOUN), radar observations. The hydrometeor PSD moments from the model output are used to derive the intercept, shape, and slope parameters for the assumed gamma distribution. Then, for each hydrometeor category, the emulator discretizes the distribution by computing the number concentration in equally spaced equivolume diameter bins from the model PSD at each grid point. Although the model hydrometeor distributions assume spherical particles, the emulator allows for variable axis ratios as a function of diameter for the purposes of the scattering-amplitude calculations. To account for wet surfaces on snow, graupel, and hail for the schemes that do not explicitly predict it, the emulator employs a diagnostic method whereby a mixture of the rain and ice fields is used to derive a water fraction on melting ice.

Improvements were made to the JXZ10 emulator for the purposes of this study. The changes mainly concern how small- to medium-sized ($D \leq \sim 2$ cm) graupel and hail particles are treated under conditions of melting or wet growth, and how the diagnosed water fraction is applied across the ice distribution. JXZ10 specified a fixed axis ratio of 0.75 for hailstones of all diameters, regardless of assumed liquid fraction, although they did provide for a decrease in the standard deviation of the canting angle with increasing liquid fraction, to account for the stabilization effects of the liquid water torus (RLP84). The laboratory investigations of RLP84, however, indicate that initially spherical hailstones of $D = \sim 1.5$ cm or less decrease rapidly in axis ratio as they melt because of the buildup of a horizontal water torus, transitioning toward the equilibrium shape of a large, approximately 8-mm raindrop, with an axis ratio of about 0.55. Kumjian and Ryzhkov (2008, p. 1944) pointed out that these ''small, wet hailstones are sensed as giant raindrops, characterized by very high Z_{DR}.'' Borowska et al. (2011) and Ryzhkov et al. (2011) accounted for these characteristics of melting hail in their polarimetric emulator by utilizing linear approximations between the aspect ratio of a dry hailstone and that of a raindrop into which it eventually melts, based on the laboratory investigations of RLP84, and by decreasing the width of the canting-angle distribution from 40°–50° for dry graupel/hail to 10° when completely melted. In our study, we follow an approach very similar to that of Ryzhkov et al. (2011) for computing the aspect ratio and width of the canting-angle distribution for melting hail with the following main differences: 1) the linear decrease of the canting-angle distribution width is applied for water fractions between 0 and 0.5 and is set to 0° above that threshold, and 2) a value of 60° is used for completely dry hail. Finally, we note that the Z_{DR} of melting hail will vary with different assumptions about axis ratios and width of the canting-angle distribution, particularly the latter. Several tests (not shown) in which these parameters were varied over reasonable ranges confirmed that the qualitative natures of the signatures were not altered. We leave further investigation of this issue to future work.

The water fraction is diagnosed via an iterative method. As a first guess, liquid water is ''borrowed'' from the q_r field and added to the q_h field up to a maximum of 90% of the rain (to avoid complete depletion of the existing rain field, which is done only for computational convenience). In the more general case of multiple ice species at a point, the rainwater is distributed among the different species weighted by their fraction of the total ice mass. We denote this borrowed or ''available'' rainwater as $q_{r,a} = 0.9q_r$. Rasmussen and Heymsfield (1987) developed a formula for the maximum or critical water mass $M_{w,\text{crit}}$ that can exist on a melting hailstone with ice core of mass M_i [see their (6)]. This is shown in Fig. 2 along with corresponding axis ratios and canting-angle widths at maximum water fraction used in the emulator.

Equation (6) of Rasmussen and Heymsfield (1987) is first rewritten as a function of the total mass of the melting hailstone $M_t = M_{w,\text{crit}} + M_i$ (where the masses are in kilograms):

$$M_{w,\text{crit}} = 2.35 \times 10^{-4} + 0.122 M_t. \quad (2)$$

Then the integration of (2) over the entire (discretized) distribution of the melting graupel or hail[3] determines

[3] For melting hail of $D < 8$ mm, the critical water fraction is actually 1.0 (RLP84)—that is, hail of sufficient size will eventually melt into a stable raindrop of $D \leq 8$ mm. Thus, for the portion of the distribution $D < 8$ mm, (2) is not used and $M_{w,\text{crit}}$ is set equal to the full mass of a hailstone of diameter D.

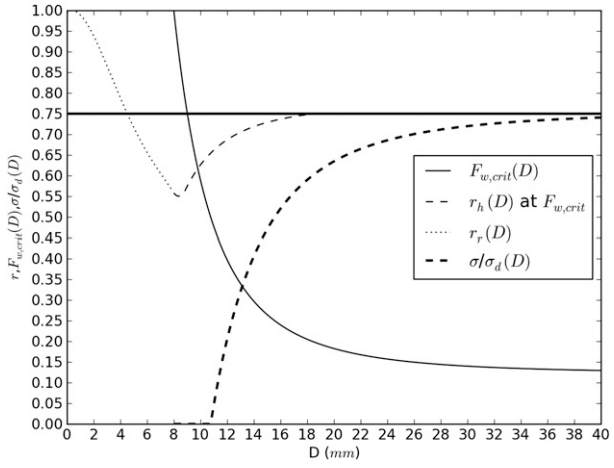

FIG. 2. Characteristics of melting hail in the polarimetric emulator: critical (maximum allowed) water fraction $F_{w,\mathrm{crit}}$ (thin black line), hail axis ratio r_h at maximum water fraction (thin dashed line), and normalized canting-angle distribution width σ/σ_d (thick dashed line), as a function of diameter of the melting particle. The ice-core density of the melting particle is assumed to be 910 kg m^{-3} for the purposes of the maximum water fraction calculation. Also shown for reference is the axis ratio of raindrops r_r as a function of diameter (thin dotted line; for diameters less than 8 mm, the fully melted hail takes on the axis ratio of the corresponding raindrop) and the assumed fixed dry hail axis ratio of 0.75 (thick black line).

the maximum water fraction allowed for the entire distribution, denoted as $F_{w,\mathrm{crit,tot}} = M_{w,\mathrm{crit,tot}}/M_{t,\mathrm{tot}}$, where the subscript tot (total) refers to the integral across the entire distribution of the corresponding quantities in (2). For the case that the available water from the rain $q_{r,a}$ exceeds $M_{w,\mathrm{crit,tot}}$, this computed $M_{w,\mathrm{crit,tot}}$ is used as the next guess of rainwater to be added to q_h and the process is iterated until convergence, eventually yielding the final diagnosed water fraction $F_w = F_{w,\mathrm{crit,tot}}$. Otherwise, the original first guess $q_{r,a}$ is used to compute $F_w = q_{r,a}/(q_h + q_{ra})$. The total number concentrations of both rain and hail are adjusted during this process to preserve their mean mass diameters. The final q_h is simply the sum of the original (dry) q_h and either the original first guess of borrowed rain $q_{r,a}$ or the final iterated $M_{w,\mathrm{crit,tot}}$, whichever is less.

After F_w for the hail distribution is determined, this available liquid water is then distributed among the discrete size bins of hail ($M_{w,i}$, $i = 1, N_{\mathrm{bin}}$, where N_{bin} is the number of discrete bins) in the following manner: 1) the ratio $R_{\mathrm{crit}} = \min(1.0, q_{r,a}/M_{w,\mathrm{crit,tot}})$ is computed and 2) $M_{w,\mathrm{crit}}$ from (2) is computed for each bin and multiplied by the ratio R_{crit}. This ensures that the available liquid water is distributed across all (discrete) hail sizes. For each bin, we also compute a local water fraction $F_{w,i} = M_{w,i}/M_{t,i}$. If $R_{\mathrm{crit}} = 1.0$, corresponding to the case that there is enough rainwater to completely "saturate" the hail distribution, then this means that for $D < 8$ mm, the hail is completely melted. In that case, these bins are simply transferred back to the corresponding bins in the rain distribution; this procedure is done to ensure the emulator treats this portion of the wet graupel and hail spectrum as rain. Thus, our diagnostic water fraction approach differs from that of Jung et al. (2008) and JXZ10 by allowing $F_{w,i}$ to vary in a physically consistent manner across the graupel and hail size distributions, instead of assuming a constant F_w applied to each bin. The above-mentioned procedure is likewise applied to the large-hail distribution if it is active.

3. 1 June 2008 supercell experiments

a. Methodology

The 1 June 2008 western Oklahoma nontornadic supercell was well observed by the KOUN S-band dual-polarized radar; its polarimetric signatures were previously documented by KRMS10, making it a case well suited for our purposes. We perform a series of idealized simulations with the NSSL Collaborative Model for Multiscale Atmospheric Simulation (COMMAS; Wicker and Wilhelmson 1995; Coniglio et al. 2006; MZB10) using a single-sounding environment described by a Rapid Update Cycle (RUC) analysis-point-proximity sounding valid 0100 UTC 1 June 2008 (Fig. 3). The overall supercell (SC) simulation naming convention is patterned after the template SC#R#[Y][X], where # represents the number of moment-weighted fall speeds used for sedimentation of rain (R) and graupel, hail-like graupel, or both graupel and large hail (Y = G, H, GLH), respectively, and X = A, B, C, D, or VD (i.e., indicating either one of the fixed bulk densities and fall speeds in Fig. 1 or variable density and fall speed are used for graupel/hail). All simulations discussed in this section are summarized in Table 2, and details are described in Table 3. A "reference" experiment [3M sedimentation with variable density graupel/hail (SC3R3HVD)] is performed along with two sensitivity experiment sets. The first set is designed to test the impact of varying fall speeds and bulk densities for the rimed-ice category, over the range of curves shown in Fig. 1, with each experiment using a fixed fall-speed curve and bulk density. The second set of experiments is designed to test the impact of size sorting of rain and graupel/hail by systematically allowing (3M sedimentation) or disallowing (1M sedimentation) size sorting in one or both categories. Results are shown at 70 min of simulation time, roughly midway between the decay of the initial convective pulse and the beginning of the decay phase of the

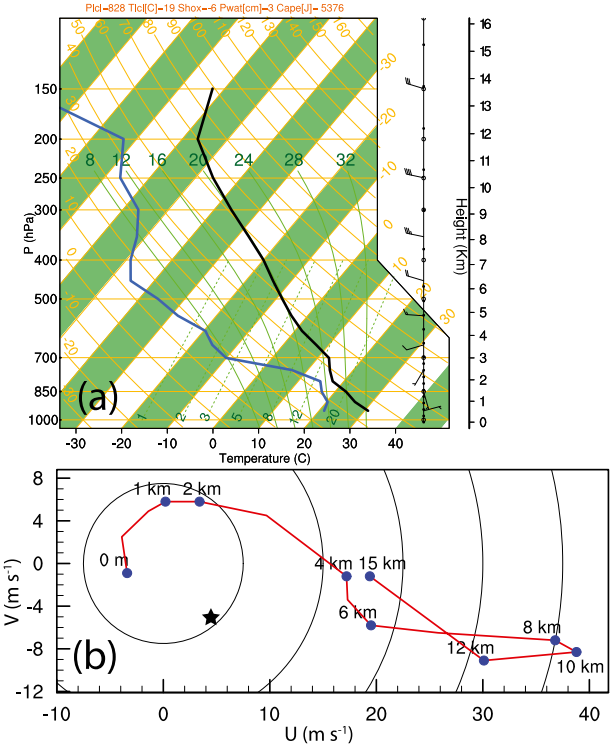

FIG. 3. The 1 Jun 2008 nontornadic supercell sounding (RUC point sounding valid at 0100 UTC): (a) skew T and (b) hodograph. The black star on the hodograph indicates the approximate observed storm motion.

storm, when the storm exhibited quasi-steady classic supercell structure similar to the observations (Fig. 4). Other times during the mature stage of the supercell (not shown) exhibit a qualitatively similar structure.

b. *Results of reference experiment*

The reference experiment (SC3R3HVD) uses the full 3M sedimentation with variable density graupel. Fields of Z, Z_{DR}, K_{DP}, and ρ_{HV} for the observed supercell and corresponding plots for experiment SC3R3HVD at 732 m AGL and 70 min are shown in Fig. 4. The simulation and observations exhibit generally good qualitative agreement in the low-level polarimetric signatures. Visible in both the observed and modeled storm is a low-Z_{DR} ($Z_{DR} < \sim 2$ dB) hail signature (hail core) in the core of the storm just northeast of the hook echo (Figs. 4c,d). However, the hail core in the simulation is offset toward the south from the location of maximum reflectivity (Fig. 4d), whereas it is close to the location of maximum reflectivity in the observations (Fig. 4c). The modeled storm Z_{DR} magnitudes (~1–1.5 dB) are also somewhat higher than the observed (~0 dB) in this region. Potential reasons for these discrepancies, all of which involve substantial uncertainty, include 1) the hail diameters may be underpredicted; 2) the observed Z_{DR} could be negatively affected by differential attenuation or nonuniform beamfilling; 3) as previously mentioned, the assumed canting-angle distribution width may be inaccurate; and 4) the assumed hail axis ratios may be inaccurate. A thorough investigation of these important issues is left to future work. A Z_{DR} arc is also apparent on the south edge of the forward flank in both the observed and modeled storms (Figs. 4c,d), although the magnitude of Z_{DR} in the arc is O(1 dB) lower in the simulation than in the observations (4.5–5 vs 5–5.5 dB), and the highest Z_{DR} (>4.5 dB) in the arc in the simulation exhibits a north–south extension that is not obvious in the observations. In addition, a secondary enhancement (relative to the surroundings) of $Z_{DR} \sim 4$ dB is apparent in both the observed and modeled storms on the northern side of the hail core, running roughly parallel to the Z_{DR} arc, which join together to the east in the forward flank. By examining the rain and hail mean volume diameters, along with the diagnosed water fraction on hail (Fig. 5), we can see that the Z_{DR} arc is in a region dominated by relatively large rain and similarly sized partially melted hail, while the hail core is indeed dominated by relatively large and dry hail.

Turning to the K_{DP} field (Figs. 4e,f), while the observations appear to be suffering from nonuniform beam filling problems in the core of the storm (near −112 km, 50 km in Fig. 4e), outside of this region the K_{DP} values and distribution in the forward flank are very similar to the simulation, with the highest K_{DP} values (>6° km^{-1}) found along the major axis of the forward flank in both cases. In the observed storm, regions of relatively low ρ_{HV} (Fig. 4g) are found juxtaposed, as expected, with low Z_{DR} in the hail core (cf. Fig. 4c), consistent with relatively large, dry, tumbling hailstones. In addition, a close examination of the ρ_{HV} field as one moves east-southeast down the forward flank near the edge shows there are still regions of moderately low ρ_{HV} (~0.95) that are collocated with high Z_{DR} associated with the Z_{DR} arc, again, in both the simulation and observations. This suggests that at least part of the observed Z_{DR} arc at this level contains a mixture of partially melted small graupel or hail and large rain, since pure rain would be expected to have $\rho_{HV} \sim 1$. In the simulations, the region of lower ρ_{HV} overlapping the Z_{DR} arc (Fig. 4h) is collocated with the region of relatively large rain and similarly sized partially melted hail (Fig. 5).

The ρ_{HV} magnitudes in SC3R3HVD are overall higher than the observations (Fig. 4h), suggesting that the model and/or polarimetric emulator is not capturing enough of the diversity in hydrometeor type or behavior. To test this from the model side, we performed another simulation, SC3R3GLHVD, which is similar to SC3R3HVD but with

TABLE 2. Summary of SC experiments using the 1 Jun 2008 environment shown in Fig. 3. Fall-speed/density labels correspond to the labeled curves in Fig. 1.

Expt identifier	Description
SC3R3GA	3M rain, 3M graupel; "A" density/fall speed
SC3R3HB	3M rain, 3M hail; "B" density/fall speed
SC3R3GC	3M rain, 3M graupel; "C" density/fall speed
SC3R3HD	3M rain, 3M hail; "D" density/fall speed
SC1R1HVD	1M rain, 1M hail; variable density/fall speeds
SC1R3HVD	1M rain, 3M hail; variable density/fall speeds
SC3R1HVD	3M rain, 1M hail; variable density/fall speeds
SC3R3HVD	3M rain, 3M hail; variable density/fall speeds
SC3R3GLHVD	3M rain, 3M graupel, 3M "large" hail; variable density/fall speeds

both the graupel/hail and large-hail categories included (hence the "GLH" in the name). Again, we present plots of Z, Z_{DR}, K_{DP}, and ρ_{HV} for this simulation in Fig. 6. The addition of the separate large-hail category has a substantial effect on ρ_{HV}, namely, lowering it to values near 0.9 in the core, closer to the observations. This can be explained simply by the added diversity in hail sizes, water fractions, and assumed tumbling characteristics by allowing two separate rimed-ice distributions to exist at a given grid point. In addition, the region of highest Z_{DR} (>4.5 dB) in the Z_{DR} arc is reduced in area from SC3R3HVD, and its orientation better approximates the observed orientation. The minimum magnitudes of Z_{DR} in the hail core are reduced to about 0.5 dB and relatively low values of Z_{DR} extend farther north toward the region of maximum reflectivity (Fig. 6b), again closer to the observations (cf. Fig. 4c). On the other hand, reflectivity magnitudes in the core are overpredicted (>70 dB), possibly because of an overprediction of hail diameters or mass mixing ratio (not shown). Testing this hypothesis is difficult, however, without direct observations of hail size distributions and precipitation rates in this case and others. In any case, a clear trend toward an improved polarimetric representation in the simulated supercell is seen when the number of rimed-ice categories is increased from one to two.

c. Results of experiments varying bulk graupel/hail density and fall speeds

To better assess the sensitivity of the low-level polarimetric features to the nature of the rimed-ice category, we next investigate the impact of a fixed density for the rimed-ice category and vary the fall-speed relations between the four labeled curves in Fig. 1. (experiments SC3R3*YX*, where Y = G, H, and X = A, B, C, or D). Neglecting the variation in density and associated fall speed for the rimed-ice category results in degraded reflectivity structure and in particular Z_{DR} signatures (Figs. 7b,d,f,h) as compared with SC3R3HVD and the observed storm (cf. Fig. 4). For the purposes of this discussion, we will mainly be focusing on the Z_{DR} field. Overall, experiment SC3R3HB (Figs. 7c,d) compares most favorably to SC3R3HVD (cf. Fig. 4), owing to the relatively high assumed fixed density (900 kg m^{-3}) and fall speeds in this experiment, which are similar to the predicted bulk density in SC3R3HVD at this level (not shown). The magnitudes of Z_{DR} in the arc with fall speed A (SC3R3GA, Fig. 7b) are substantially reduced relative to that of SC3R3HVD (cf. Fig. 4) because of the presence of relatively dry, large graupel (Fig. 8b, $D_{mg} \sim$ 8–12 mm) in SC3R3GA, whereas SC3R3HVD instead has relatively wet, smaller hail (Fig. 5b, $D_{mh} \sim$ 5–6 mm). This difference may be a consequence of the relatively low fixed density assumed (500 kg m^{-3}) that results in larger D_{mg} for the same q_g and N_{Tg}, as well as the lower fall speeds relative to SC3R3HVD and more downstream transport for a given D_{mg}. The larger D_{mg} in this region also causes less water to be diagnosed on the graupel surface (Fig. 9a, also true for SC3R3GC in Fig. 9c) compared to the higher-density hail experiments (SC3R3HB and SC3R3HD, Figs. 9b,d, respectively). This in turn results in lower Z_{DR} (because the larger, drier graupel tumbles more).

TABLE 3. Idealized simulation characteristics.

Domain size	100 km × 100 km (horizontal), 20 km (vertical)
Grid spacing	1 km horizontal; stretched from 200 m at the bottom to 500 m at the top in the vertical; 50 vertical levels
Boundary conditions	Open lateral; free-slip bottom and top
Time step	4 s (large), 2/3 s (small)
Radiation, surface physics, Coriolis force	None
Subgrid-scale turbulence parameterization	1.5-order prognostic turbulent kinetic energy (TKE) closure
Microphysics	NFD and NVD MM scheme (Ziegler 1985; MZB10)
Convective initiation procedure	Updraft nudging (Naylor and Gilmore 2012) to 10 m s^{-1} applied over the first 900 s in an ellipsoidal region (30 km × 30 km × 6 km); center placement at 40 km × 40 km × 1.5 km relative to southwestern corner of domain

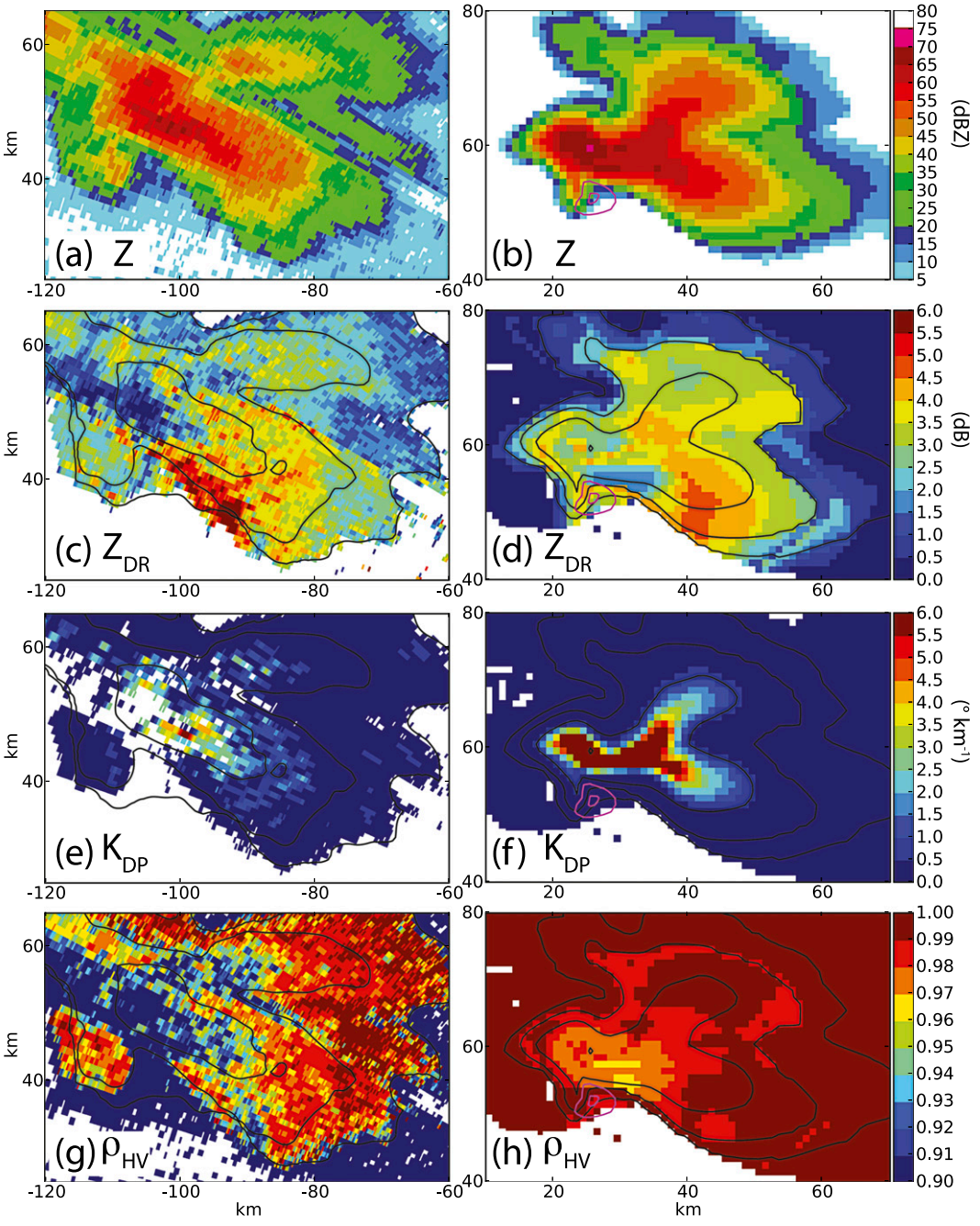

FIG. 4. (left) Representative radar images of the 1 Jun 2008 northwestern Oklahoma nontornadic supercell (0.0° elevation, valid 0255:43 UTC) from the KOUN dual-polarized radar: (a) reflectivity at horizontal polarization, (c) differential reflectivity, (e) specific differential phase, and (g) cross-correlation coefficient. (b)–(d) The reflectivity contours in 20-dBZ increments, starting at 10 dBZ (black), are overlaid. (right) As in (left), but for experiment SC3R3HVD at 4200 s and about 732 m AGL. Thin magenta contours indicate vertical velocity at about 3 km AGL in 10 m s^{-1} increments, starting at 10 m s^{-1}.

In keeping with this trend, fall speed C (SC3R3GC) exhibits an unrealistically large forward-flank region with a Z_{DR} arc that is "smeared" over a large east-to-west extent (Fig. 7f) as compared with the observations (cf. Fig. 4b). Again, this result is a consequence of the even lower fall speeds for graupel assumed in this experiment (cf. curve C in Fig. 1). The relatively slow increase of graupel terminal fall speed V_{tg} with diameter

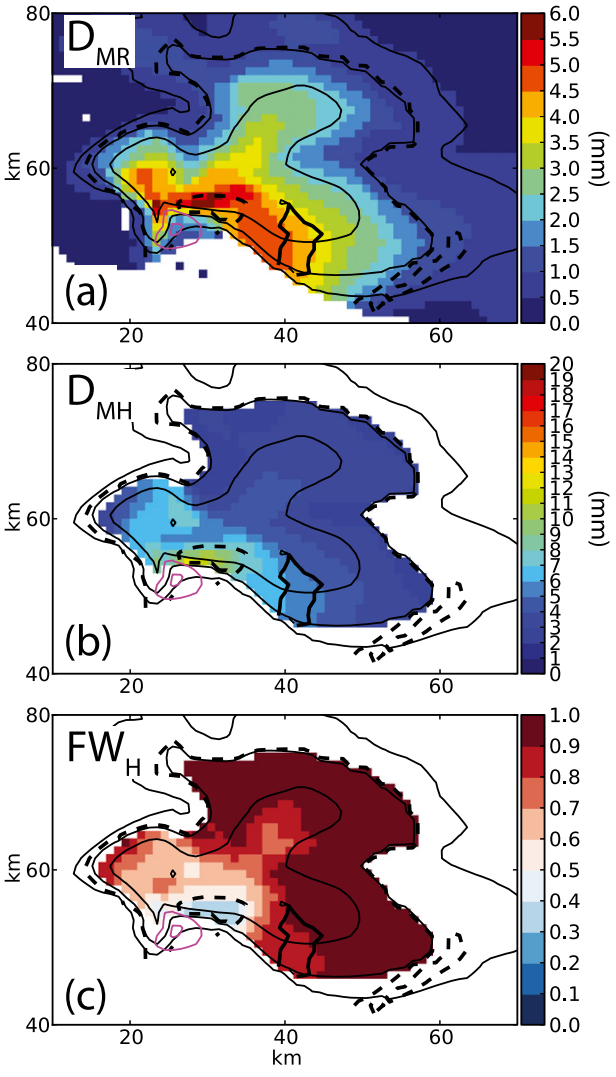

FIG. 5. As in Fig. 4 (right), but for (a) rain mean volume diameter D_{mr}, (b) hail mean volume diameter D_{mh}, and (c) fraction of liquid water on hail F_{wh}. Thin black contours indicate reflectivity (20-dBZ increment, starting at 10 dBZ). The thick solid (dashed) contour indicates Z_{DR} = 4.5 (2.0) dB. Thin magenta contours indicate vertical velocity at about 3 km AGL with a 10 m s^{-1} increment, starting at 10 m s^{-1}.

for this curve also means that less size sorting can occur over a given range of graupel diameters and explains the relatively broad gradients in D_{mg} (Fig. 8f). Finally, experiment SC3R3HD exhibits Z_{DR} signatures (Fig. 7h) somewhat intermediate between the low-density, slow-falling graupel experiment (SC3R3GA, Fig. 7b) and the high-density, fast-falling hail experiment (SC3R3HB, Fig. 7d), again because of lower fall speeds assumed (cf. curve D and curve B in Fig. 1).

To summarize, the fall-speed curve and bulk density for graupel or hail have profound impacts on the resulting low-level polarimetric signatures in the simulated supercell: the higher-density, faster-falling hail-like species generally result in polarimetric signatures that are closer to the polarimetric observations for this case than the lower-density, slower-falling graupel-like species, when compared to the variable density reference simulation and the observed signatures.

d. Results of size-sorting experiments

Next we examine the experiment sets that use either a single (1) mass-weighted fall speed for sedimentation (i.e., size-sorting disabled, as in SC1R1HVD) or the three (3) appropriately weighted fall speeds for each of the predicted moments (i.e., size-sorting enabled, as in SC3R3HVD). In general, as one goes from disallowing size sorting completely (SC1R1HVD, first rows in Figs. 10–12) to allowing it for both rain and hail (SC3R3HVD, last rows in Figs. 10–12), there is a substantial improvement in the fidelity of the Z_{DR} signatures (Fig. 10, right) as compared with observations (cf. Fig. 4, left). In contrast, the reflectivity structure (Fig. 10, left) and K_{DP} fields (Fig. 11, left) are relatively insensitive to these changes across experiments; Z_{DR} does not depend directly on the total hydrometeor mass at a given grid point, but it does strongly depend on hydrometeor properties (such as oblateness or tumbling characteristics) that themselves depend on the PSD. In contrast K_{DP} depends strongly on the total hydrometeor mass and to a lesser extent the PSD, while Z depends strongly on both. This additional dependence on hydrometeor mass may help explain the overall lack of sensitivity (especially in K_{DP}) to size sorting, which strongly modifies the PSD.

The two experiments that disallow sorting in the hail field (SC1R1HVD and SC3R1HVD, first two rows in Figs. 10–12) exhibit relatively poor agreement in the Z_{DR} field with the observed structure, with broad, relatively weak gradients in Z_{DR} over most of the forward flank (Figs. 10b,d), and little evidence of an enhanced Z_{DR} arc or low-Z_{DR} hail core. In addition, the ρ_{HV} field displays a broader region of magnitudes less than 1 than the other experiments (cf. Figs. 11b,d and Figs. 11f,h), which is due to the broader region of (relatively small) graupel in the forward flank. The former is reflected in the D_{mh} field in both experiments (Figs. 12b,d), which displays relatively small values (2–4 mm, close to the average value aloft, not shown) and weak gradients. In SC3R1HVD, the effects of rain sorting are evident with a general south-to-north decrease in D_{mr} in the forward flank (Fig. 12c), but this has little overall impact on the Z_{DR} field, likely due to the contribution from hail. In contrast, SC1R3HVD (Figs. 10–12, third rows) is very similar to the reference simulation SC3R3HVD

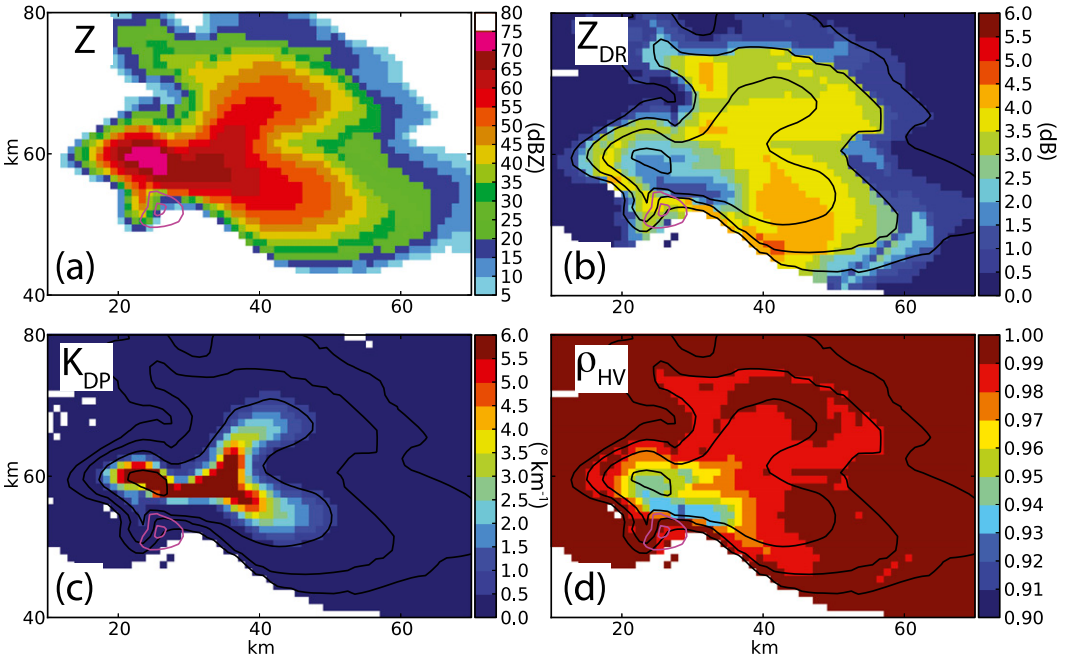

FIG. 6. As in Fig. 4, but for experiment SC3R3GLHVD, which includes separate variable-density graupel and hail categories.

(Figs. 10–12, bottom rows) in regard to the presentation of the Z_{DR} arc and low-Z_{DR} hail signature, and both compare favorably to observations (cf. Fig. 4c). The ρ_{HV} in the hail core in these simulations (Figs. 11f,h) is also lowered relative to the no-hail-sorting runs (Figs. 11b,d), in closer agreement with observations (Fig. 4g).

Even though the rain field is not allowed to sort in SC1R3HVD, the pattern of D_{mr} is remarkably similar to SC3R3HVD (Figs. 12e,g). This strongly suggests that sorting in the hail field is the dominant factor in controlling the location of the largest raindrops and associated polarimetric radar presentation, at least in regard to the Z_{DR} arc and Z_{DR} hail-core signature. However, Z_{DR} (Fig. 10f) is somewhat overpredicted on the northwestern flank of the storm as compared with both SC3R3HVD (Fig. 10h) and the observations (Fig. 4c). This result is reflected in the D_{mr} field, which shows larger D_{mr} in this region in SC1R3HVD (Fig. 12e) than in SC3R3HVD (Fig. 12g). Thus, while size sorting in the graupel/hail category appears most important in regard to the two main signatures of interest to this study, there is a noticeable impact from rain sorting as well in the overall Z_{DR} presentation. Finally, we again note that in both SC1R3HVD and SC3R3HVD, a secondary region of enhanced Z_{DR} (relative to the surroundings) north and northeast of the hail core is evident. This signature is a result of a mixture of relatively small, partially melted hailstones that have "sorted out" on the northern side of the hail core and similarly sized large raindrops. This northern enhancement of Z_{DR} can be viewed as representing a "transition zone" between the relatively large, dry hail to its immediate south and progressively smaller raindrops and completely melted hailstones to its north.

4. 3D sedimentation experiments

a. Methodology

Although the impact of size sorting of rain and graupel/hail on forward-flank polarimetric signatures is evident in the full supercell experiments, we can investigate their impacts in a more simplified framework that better reveals the underlying physics. To this end, we perform four idealized experiments—mirroring those of the size-sorting supercell experiments above—wherein a constant hail source at the top boundary (set at 12 km AGL) is imposed, and the hail falls and melts in the same horizontally homogeneous background wind and thermodynamic profile as used for the supercell experiments (Fig. 3). These experiments are identified by the naming template 3D#R#HVD with the same convention as used previously, and are summarized in Table 4. Horizontal and vertical grid spacings are constant at 500 and 200 m, respectively. Based on the reference supercell experiment (SC3R3HVD), we impose a constant circular source region of hail at the 12-km level utilizing a cosine-squared

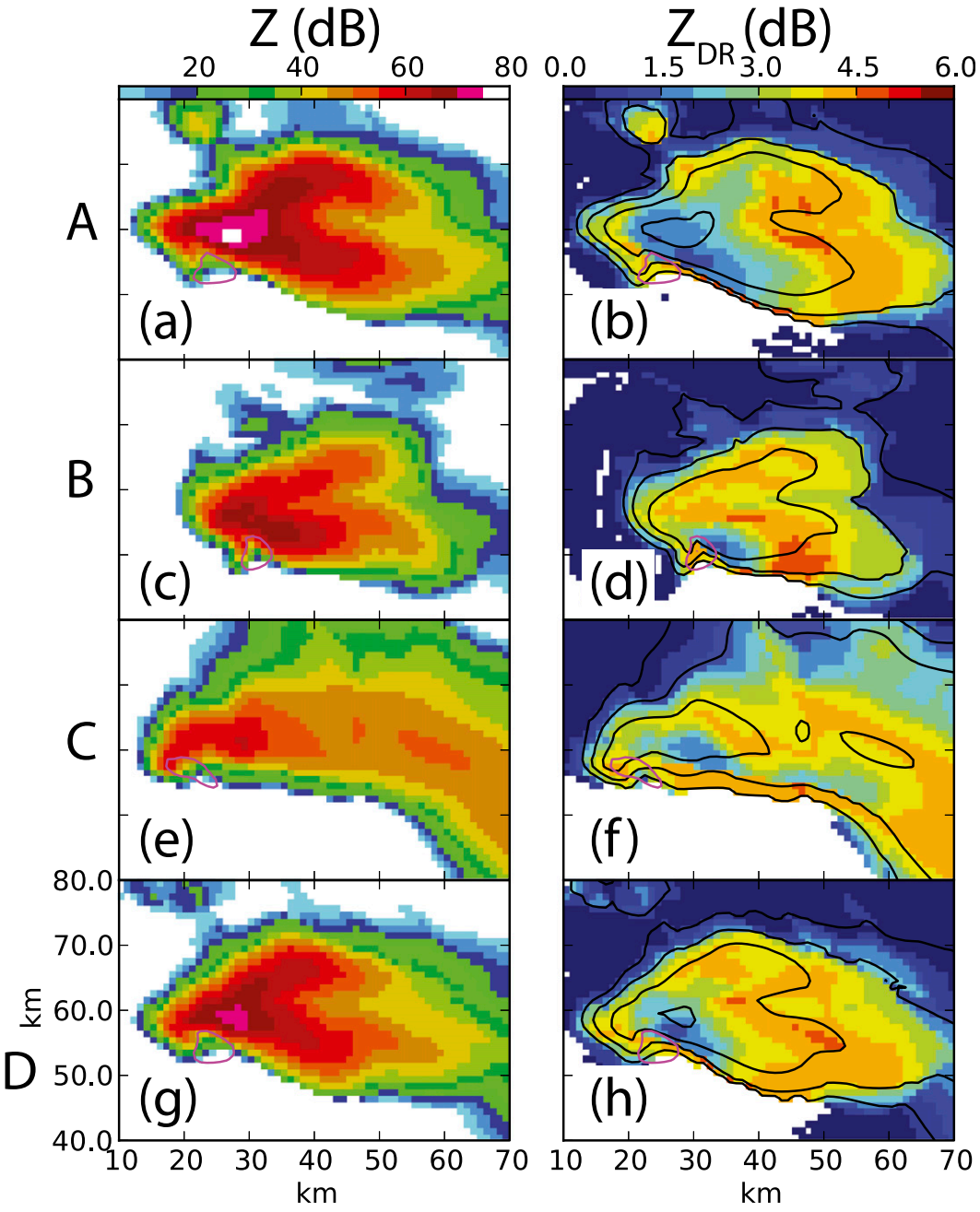

FIG. 7. (left) Reflectivity Z (color fill, dBZ) and (right) differential reflectivity Z_{DR} (color fill, dB) for (a),(b) SC3R3GA, (c),(d) SC3R3HB, (e),(f) SC3R3GC, and (g),(h) SC3R3HD. Reflectivity in 20-dBZ increments, starting at 10 dBZ, is overlaid with black contours in (right), and vertical velocity with a 10 m s^{-1} increment is overlaid with magenta contours in each panel. Each row is labeled by the corresponding fall-speed curve and graupel/hail bulk density used and labeled as in Fig. 1.

function for q_h, with a maximum of 8 g kg^{-1} in the center. The mean volume diameter D_{mh} is set to a constant 2 mm, the gamma shape parameter is set to zero, and the initial bulk density is set to 800 kg m^{-3}. The top boundary source region is assumed to be moving with the same speed and direction as the simulated supercell (black star in Fig. 3). While the hail is allowed to fall and melt into rain, for simplicity no dynamic or thermodynamic feedback to the environment is allowed. The simulations are run out to 1800 s, which was found to be sufficient to reach a steady state in all cases. Our goal is to produce a simplified model of the forward-flank precipitation

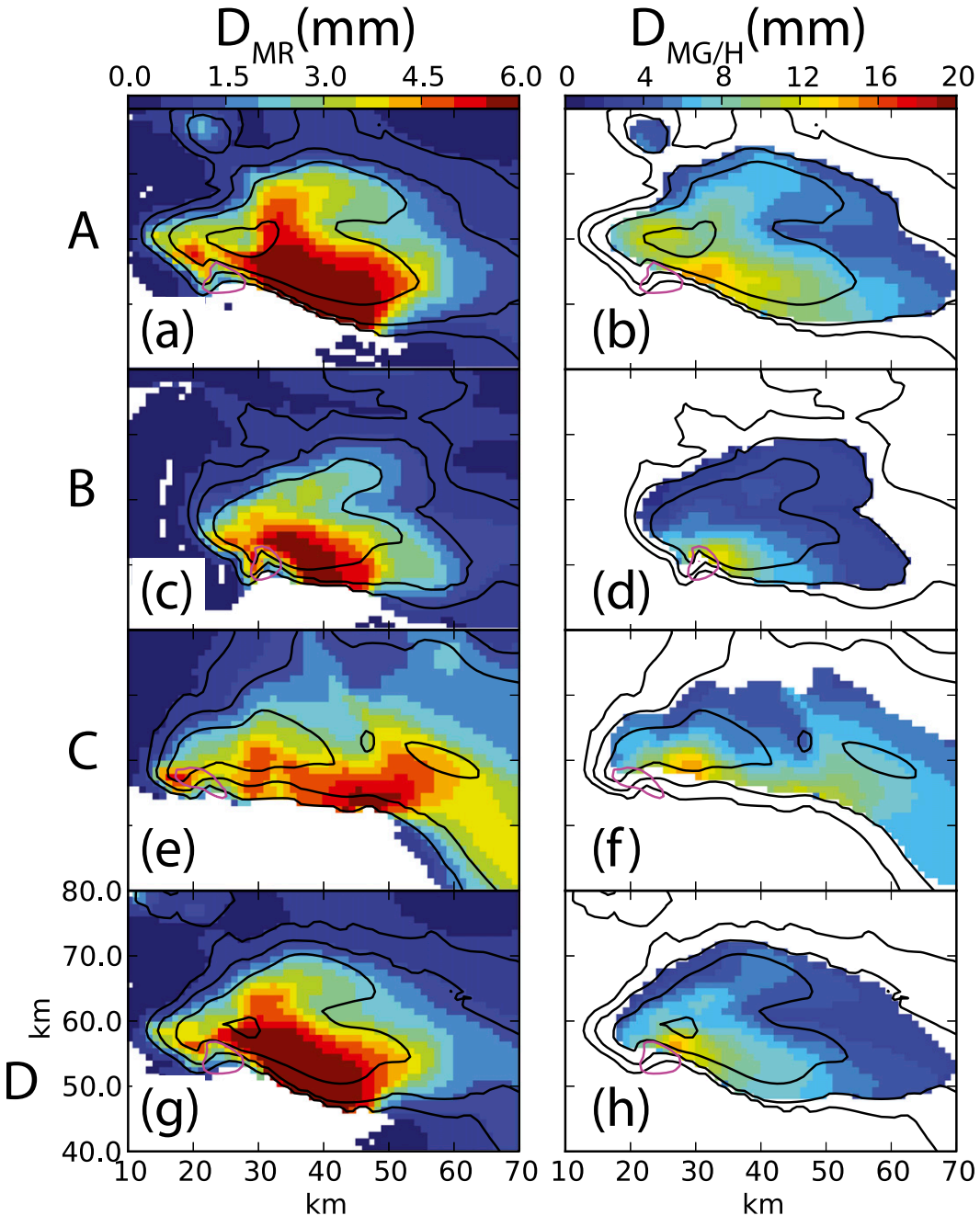

FIG. 8. As in Fig. 7, but for (left) rain mean volume diameter D_{mr} (color fill, mm) and (right) graupel/hail mean volume diameter $D_{mg/h}$.

region of supercells removed from the main updraft, in which vertical motions play a relatively minor role, and sedimentation and melting of hail into rain in the presence of substantial environmental wind shear are presumably the most important microphysical processes.

We emphasize here that we do not wish to discount the importance of size sorting by the storm updraft in the region of the updraft itself, a mechanism examined in previous studies (e.g., MY05a; KR12). It is well known that maximum hail sizes are strongly correlated with updraft strength, and the maxima in $D_{mg/h}$ in the supercell experiments are indeed close to the updraft region (see magenta contours in Figs. 5b and 8, right). The updraft thus influences the initial sizes and distribution of graupel and hail aloft before the particles fall out and advect downstream into the forward flank. Our analysis

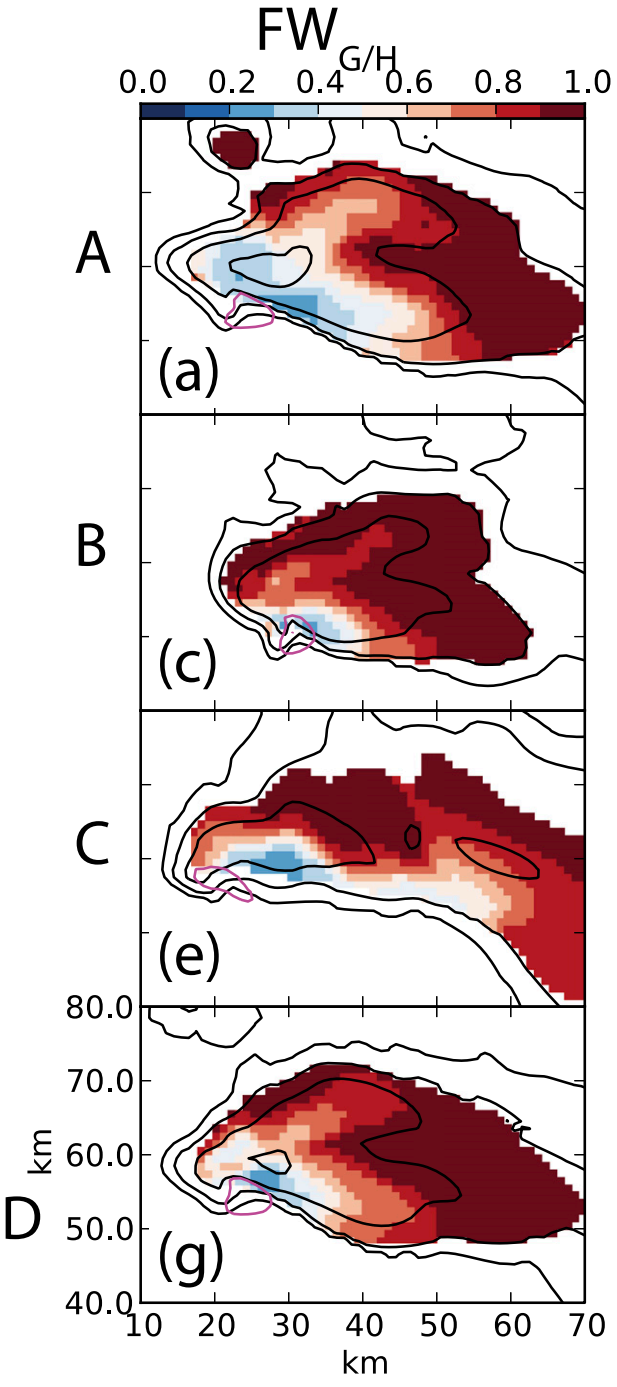

FIG. 9. As in Fig. 7, but for fraction of liquid water on graupel/hail $F_{wg,h}$.

is instead concerned with the further sorting of graupel and hail once it is carried downstream of the updraft region (outlined by magenta contours in Figs. 4–11) into the broad forward flank. Throughout this section, we analyze horizontal cross sections at 700 m AGL through the precipitation shafts, a height at which the Z_{DR} arc in a supercell would be expected to be apparent. For brevity, we will focus on the Z and Z_{DR} fields in the following analysis.

b. Results

We see the same basic patterns in Z, Z_{DR} (Fig. 13), D_{mr}, and D_{mg} (Fig. 14) as in the corresponding full supercell experiments, which lends support to our hypothesis that size sorting of graupel/hail is the dominant mechanism modulating the distinct Z_{DR} signatures identified previously, at least in the forward-flank region, with additional effects from rain size sorting. In particular, both 3D3R3HVD and 3D1R3HVD have very similar Z_{DR} signatures (Figs. 13f,h), respectively, with the main difference being in the northern third of the precipitation shaft, where 3D1R3HVD has higher Z_{DR} (Fig. 13f) associated with larger D_{mr} (Fig. 14e) than in 3D3R3HVD (Figs. 13h and 14g, respectively). This difference is due to the lack of size sorting of rain in 3D1R3HVD, corresponding well to the results from the supercell experiments discussed previously.

Referring to the rain terminal velocity curve in Fig. 1, one sees that the fall speed is nearly constant for rain diameters larger than about 4 mm, and thus limited size sorting among these larger drops will occur, whereas substantial size sorting of these drops relative to drops smaller than about 4 mm will indeed occur. This explains why the high-Z_{DR} region on the southeastern flank of the idealized precipitation shaft—where the distribution is dominated by larger drops—in 3D1R3HVD and 3D3R3HVD is so similar, and accordingly why the greatest impact from size sorting on rain occurs in the smaller-drop region in approximately the northern third of the shaft. More specifically, in the area of highest Z_{DR} (>4.5 dB) centered near the coordinates (22, 20) km in Fig. 13h, the hail is nearly completely melted (not shown) and D_{mh} approaches that of large raindrops (~6–8 mm, Figs. 14f,h). In the same area, D_{mr} is near its maximum allowed size (6 mm, Figs. 14e,g). This juxtaposition of nearly completely melted, small wet hail, and large raindrops is what ultimately explains the high Z_{DR} in this region.

Additional insight is gained when we examine the gradients of the mean volume diameter of hail and rain and compare them with the storm-relative mean wind over the entire depth of the precipitation shaft, and over the depth of the submelting layer (defined by the wet-bulb zero level of about 3 km), respectively. When only hail is allowed to sort (3D1R3HVD, Figs. 13, 14, third rows), the gradients of D_{mh} and D_{mr} align in a similar direction, close to the direction of the mean storm-relative wind vector in the 0.7–12-km layer (magenta vectors in Fig. 14). When instead only rain is allowed to sort

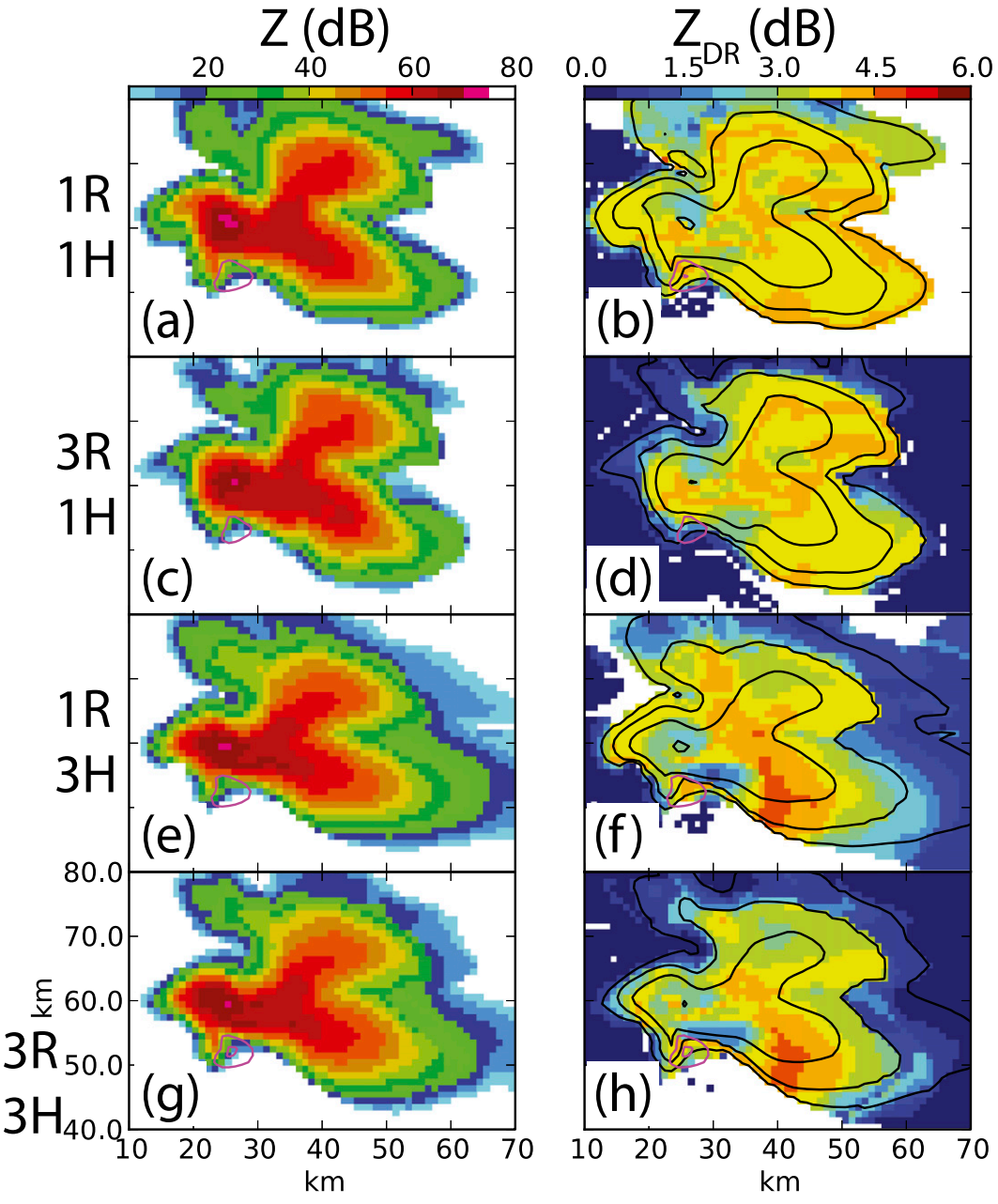

FIG. 10. As in Fig. 7, but for the SC#R#HVD suite of simulations. The number of sedimentation moments for rain and hail predicted in each experiment is labeled to the left of each row.

(experiment 3D3R1HVD, Figs. 13, 14, second rows), the gradient in the D_{mr} field (Fig. 14c) aligns more closely with the submelting-level (0.7–3 km) mean storm-relative wind vector (black vectors in Fig. 14). When both hail and rain are allowed to sort (3D3R3HVD, Figs. 13, 14, bottom rows), the situation is very similar to 3D1R3HVD, except that the gradient in D_{mr} is shifted slightly toward the direction of 0.7–3-km storm-relative mean wind vectors (cf. Figs. 14g,e).

c. *Comparison with supercell experiments*

This basic situation is also evident in the full supercell experiments, as can be seen by examining the storm-relative mean wind vectors for the deep (magenta) and shallow (black) layers for each of the size-sorting experiments (Fig. 12). In the supercell simulations, however, perturbations to the environmental wind profile by the storm itself are reflected in a spatial variation of

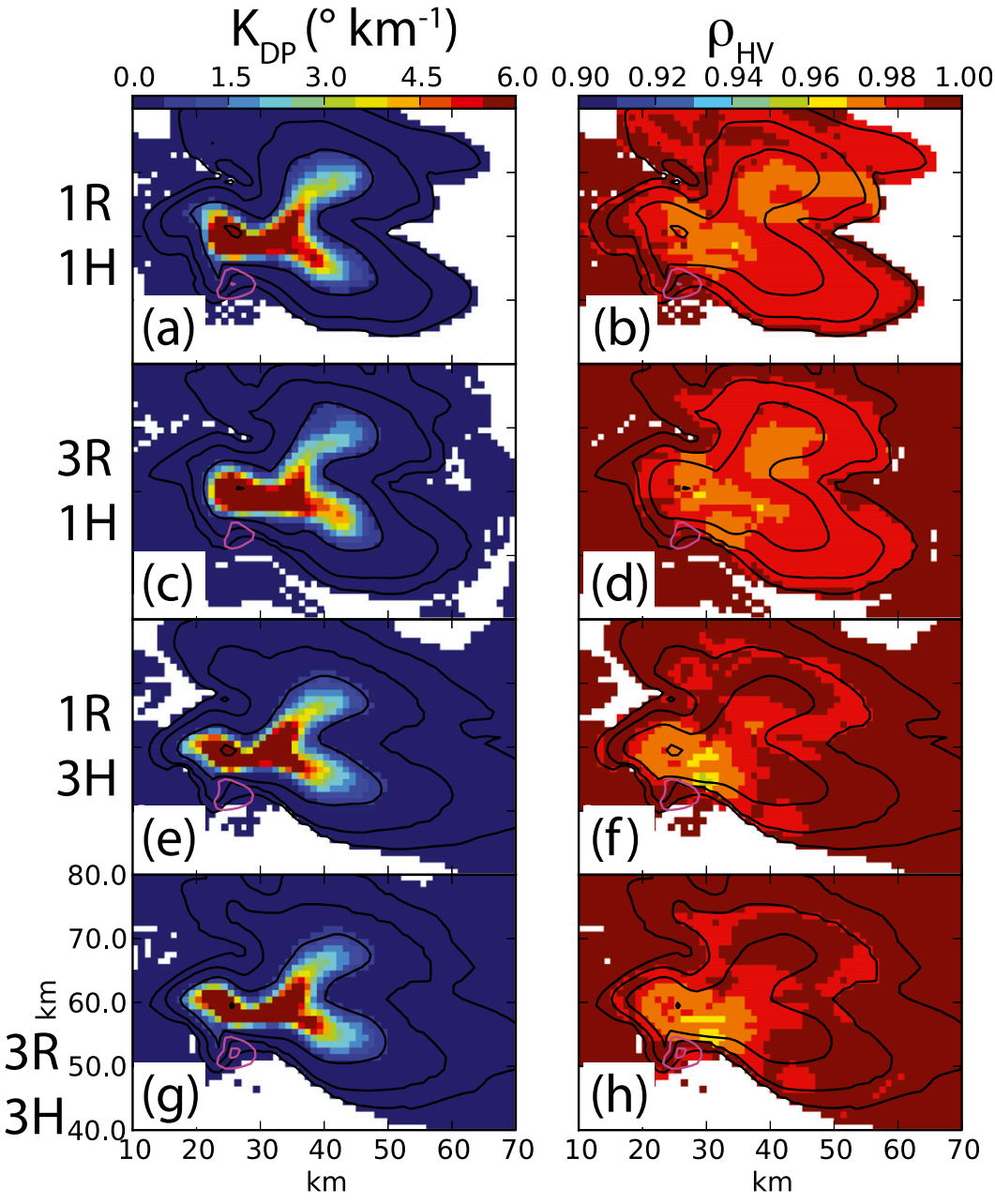

FIG. 11. As in Fig. 10 but for (left) K_{DP} and (right) ρ_{HV}.

these mean wind vectors across the storm (cf. vectors in Fig. 12). This, in turn, results in a spatially varying size-sorting pattern. Four hodographs from SC3R3HVD representing the base-state wind profile, wind within the hail core, wind within the Z_{DR} arc, and wind north of the Z_{DR} arc are shown in Fig. 15a–d, respectively, along with the aforementioned low-level and deep-layer storm-relative mean wind vectors (locations are denoted by yellow circles in Fig. 12h). The hail-core hodograph (Fig. 15b) exhibits strong backing and enhancement of the low- to midlevel winds relative to the others owing to its location near the mesocyclone in the strong inflow (also mentioned by KR09 as potentially enhancing the amount of size sorting in this region). This backing is associated with a more north–south and sharper gradient in D_{mh} evident near this location (Fig. 12h). The other hodographs in and near the Z_{DR} arc farther downstream from the updraft and mesocyclone (Figs. 15c,d) are more similar to the base-state wind profile (Fig. 15a). Finally, vertical cross sections of D_{mh} (gray

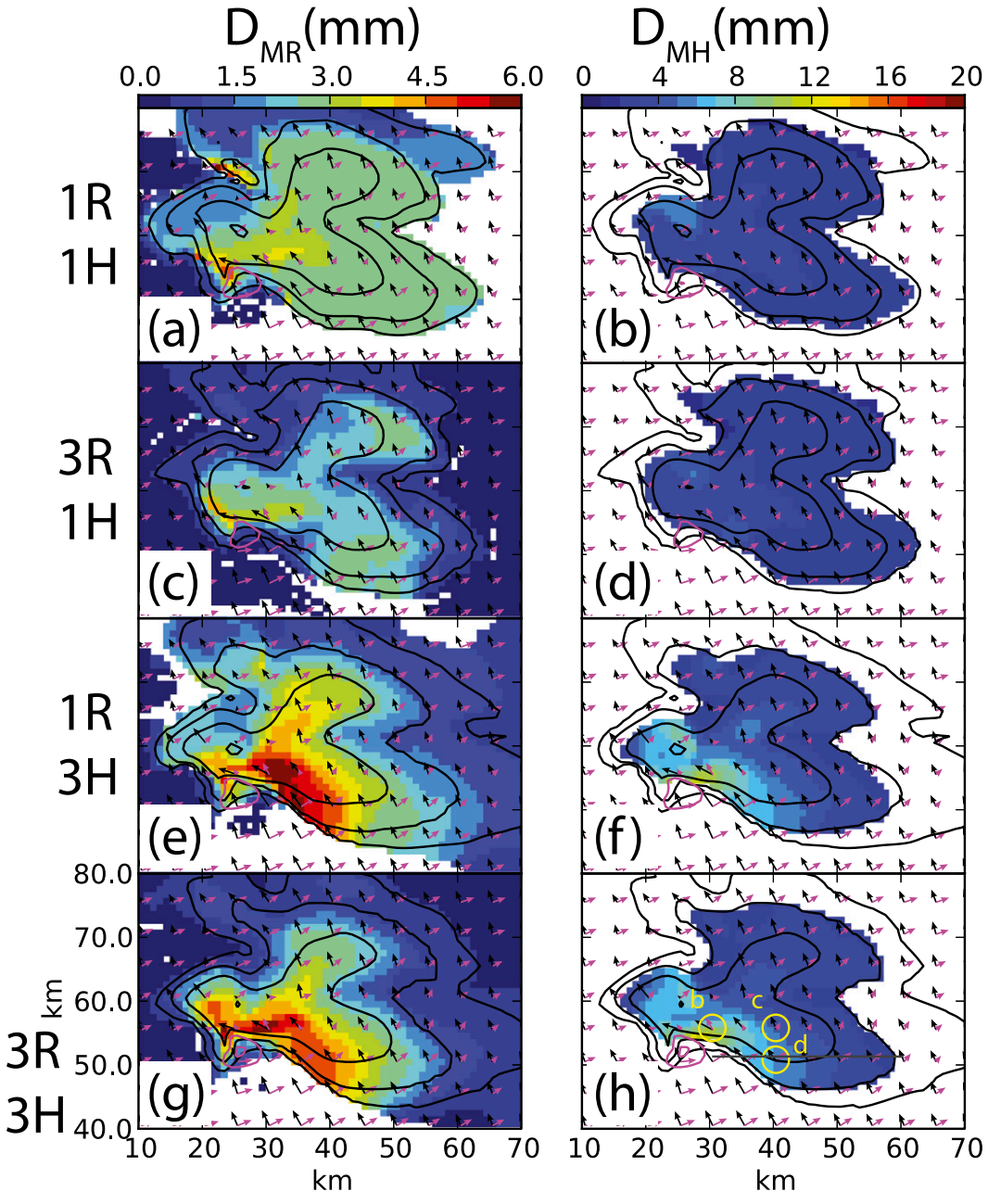

FIG. 12. As in Fig. 10, but for (left) rain mean volume diameter D_{mr} (color fill, mm) and (right) hail mean volume diameter D_{mh} (color fill, mm). The 0.7–3- (black) and 0.7–12-km (magenta) storm-relative mean wind vectors are overlaid with a 5-km increment. The yellow circles and labels in (h) refer to three vertical wind profiles shown in the corresponding panels of Fig. 15, while the gray line represents the location of the vertical cross section shown in Fig. 16a.

lines in Figs. 12h and 14h) through the southern portion of the precipitation shaft, transecting the Z_{DR}-arc region in both SC3R3HVD and 3D3R3HVD, are shown in Fig. 16, indicating that substantial sorting of hail indeed occurs in the forward-flank region above the melting level (~3 km AGL) because of the storm-relative winds in this upper layer in each case.

Thus, the overall pattern in D_{mr} and D_{mh} in SC3R3HVD and the other SC experiments is similar to the corresponding idealized sedimentation experiments, especially in the southern portion of the forward flank, where the storm-relative mean wind vectors are most similar to their undisturbed environmental counterparts. These patterns in D_{mr} and D_{mh} are reflected in an overall slight

TABLE 4. As in Table 1, but for the 3D sedimentation experiments.

Expt identifier	Description
3D1R1HVD	1M rain, 1M hail; variable density/fall speeds
3D1R3HVD	1M rain, 3M hail; variable density/fall speeds
3D3R1HVD	3M rain, 1M hail; variable density/fall speeds
3D3R3HVD	3M rain, 3M hail; variable density/fall speeds

shift in the higher Z_{DR} toward the downwind (in the deep-layer mean sense)-right side of the precipitation shaft for 3D3R3HVD (Fig. 13h), relative to 3D1R3HVD (Fig. 13f).

We also note in the Z_{DR} field for 3D1R3HVD and 3D3R3HVD, an area of low Z_{DR} on the upwind side of the precipitation shaft (Figs. 13f,h) that is reflective of the largest D_{mh} and thus PSDs dominated by relatively large and dry hail (Figs. 14f,h, and 16b). Comparing with the observed storm structure for this case (Fig. 4c), one can see a qualitative agreement in the relative locations and magnitudes of the low-Z_{DR} hail core and the Z_{DR} arc. Finally, it is worth noting again that disabling size sorting for hail substantially degrades the low-level Z_{DR} field as compared with the observations; large and dry hail is not allowed to "sort out," leading to a muted or

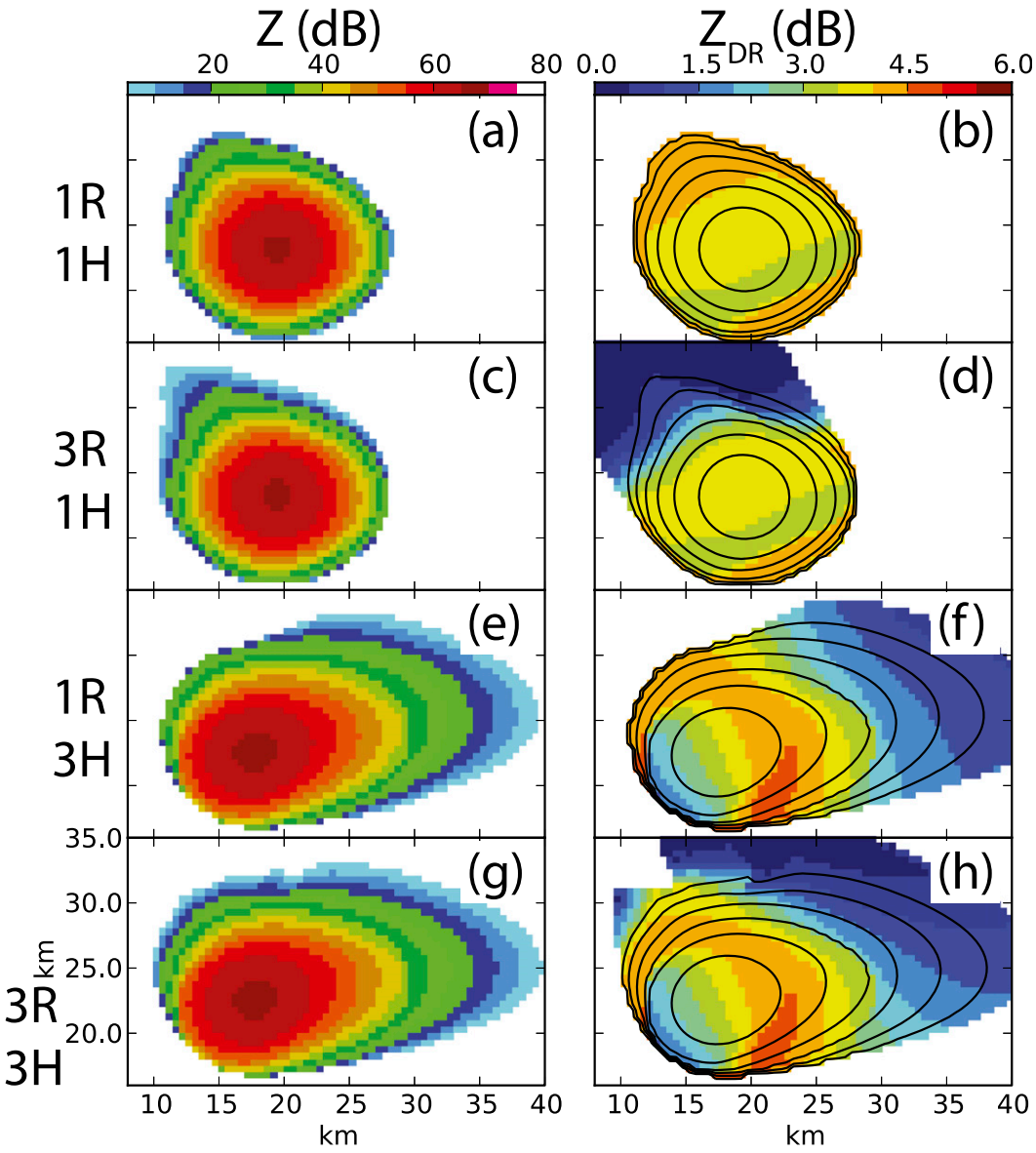

FIG. 13. As in Fig. 10, but for the idealized steady 3D sedimentation size-sorting experiments (3D#R#HVD, where # is the number of sedimentation moments) at 1800 s and 700 m AGL.

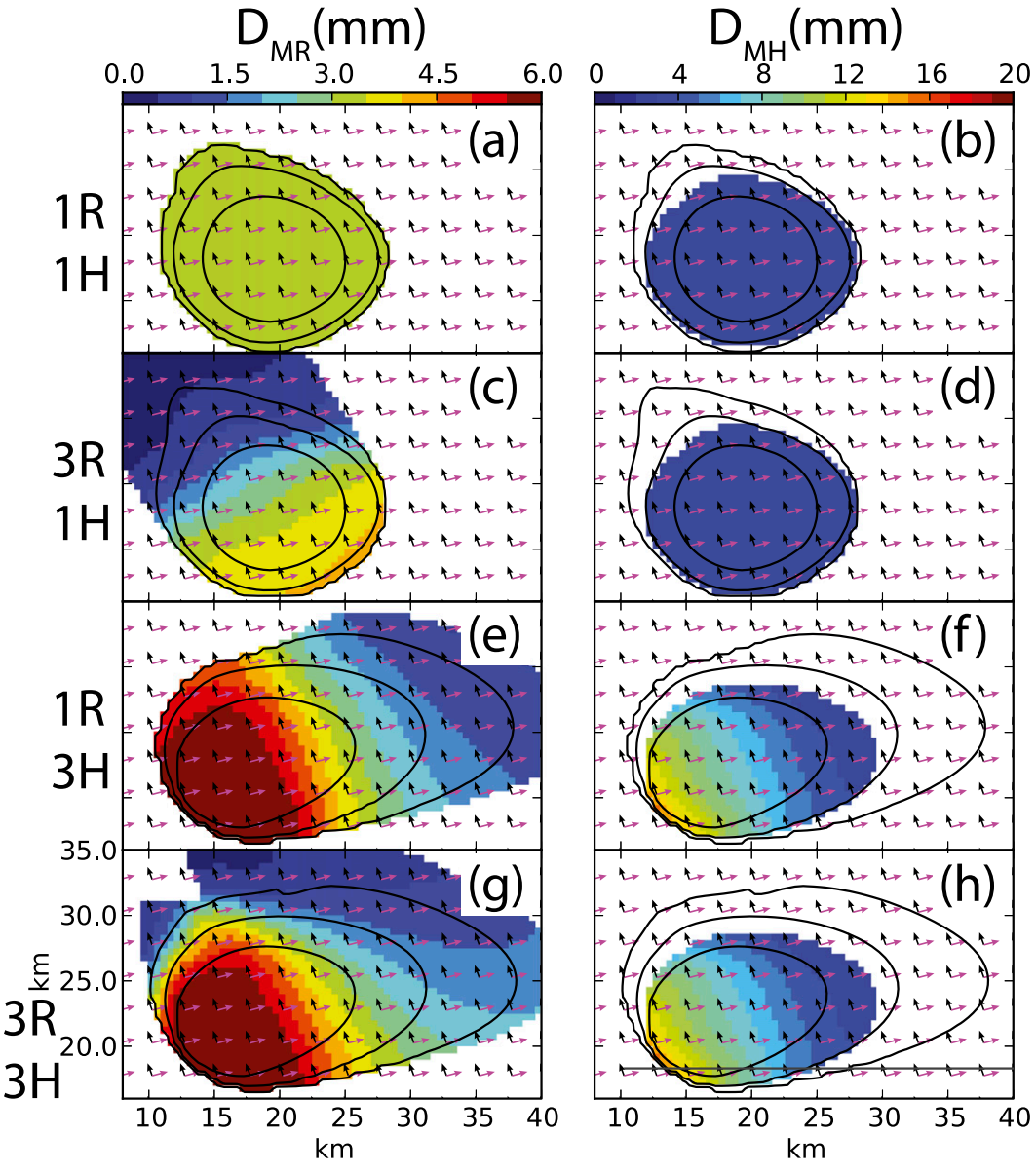

FIG. 14. As in Fig. 12, but for the 3D#R#HVD experiments. The gray line in (h) denotes the location of the vertical cross section shown in Fig. 16b.

absent low-Z_{DR} hail signature in the low levels (Figs. 10, 13b,d). We note in passing that this latter result is sometimes observed in tornadic storms (Kumjian and Ryzhkov 2008).

5. Summary and conclusions

This study investigated the impact of size sorting of hail and rain in the presence of environmental shear on the qualitative nature of the resulting low-level polarimetric fields (with an emphasis on Z_{DR}) in supercell forward flanks through the use of numerical simulation and a polarimetric radar emulator operating on the model microphysics-state variables. The goals were to 1) characterize features in the simulated polarimetric fields; 2) explain the physical cause of these features as a function of size sorting and melting behavior; and 3) broadly compare them with observed features, particularly the Z_{DR} arc or shield commonly observed in the forward-flank region of supercell thunderstorms, and the classic low-Z_{DR} hail signature near the storm reflectivity core. The aforementioned goals were accomplished by systematically investigating a series of idealized supercell and simple precipitation shaft simulations using

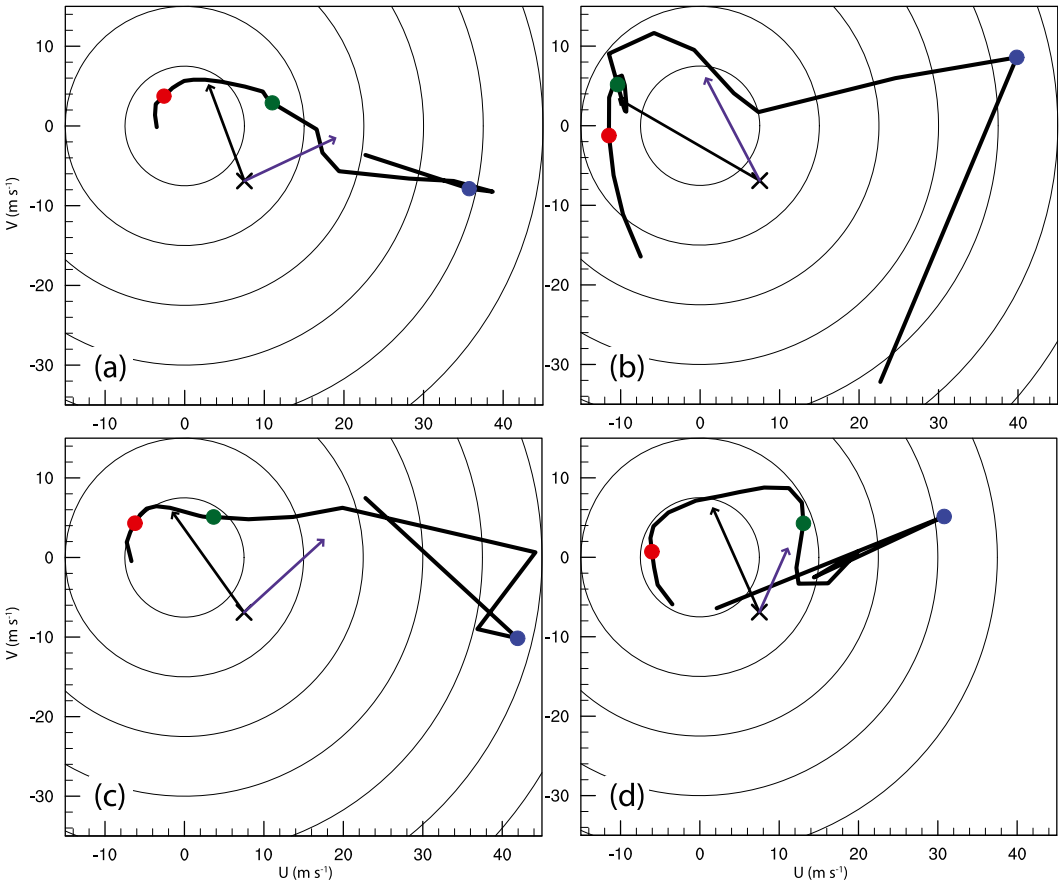

FIG. 15. Hodographs (black lines), 0.7–3-km mean storm-relative wind vectors (black arrows), and 0.7–12-km mean storm-relative wind vectors (purple arrows) at 4200 s in simulation SC3R3HVD (a) for the base-state wind profile, (b) near the center of the hail core, (c) within the Z_{DR} arc, and (d) north of the Z_{DR} arc; (b)–(d) are labeled as in Fig. 12h. The red, green, and blue dots denote the 700-m, 3-km, and 12-km winds, respectively. The storm motion vector is labeled by a cross at the tail of the storm-relative wind vectors. Circles are plotted every 7.5 m s^{-1}.

a triple-moment bulk microphysics scheme and varying assumptions about the graupel/hail bulk density and fall speeds, and determining whether size sorting was allowed in the hail and/or rain fields.

From the results of the numerical experiments, we make the following specific observations and conclusions:

1) The Z_{DR} presentation of simulated supercell forward flanks below the melting level depends strongly on the characteristics of graupel/hail in the model microphysics scheme. In particular, variation of the fall speed and bulk density has a profound effect on the resulting Z_{DR} signatures. When the rimed-ice category is more graupel like, the forward-flank region is too broad, gradients in Z_{DR} are weak, and the low-Z_{DR} hail-core signature is too expansive, restricting or masking the Z_{DR} arc. However, when the rimed-ice category is more hail like, the Z_{DR} arc and a low-Z_{DR} hail core that is much closer to the observations in size, magnitude, and location are produced. The results most consistent with the observations in this case are obtained for the full triple-moment scheme with separate graupel/hail and large-hail categories and predicted bulk density and fall speeds.
2) The low-level Z_{DR} signatures in simulated supercell forward flanks are strongly modulated by sustained size sorting by the storm-relative winds. Although size sorting in both the rain and graupel/hail fields is important, it is the sorting of the graupel/hail fields that has greater impact on simulating both the Z_{DR} arc and hail core. Sorting of the rain field mainly modulates the Z_{DR} magnitudes on the left flank of the (right moving) supercell. These findings extend the arguments of previous studies investigating the size-sorting mechanism in the development of the Z_{DR} arc by implicating sorting of hail and graupel over that of rain.

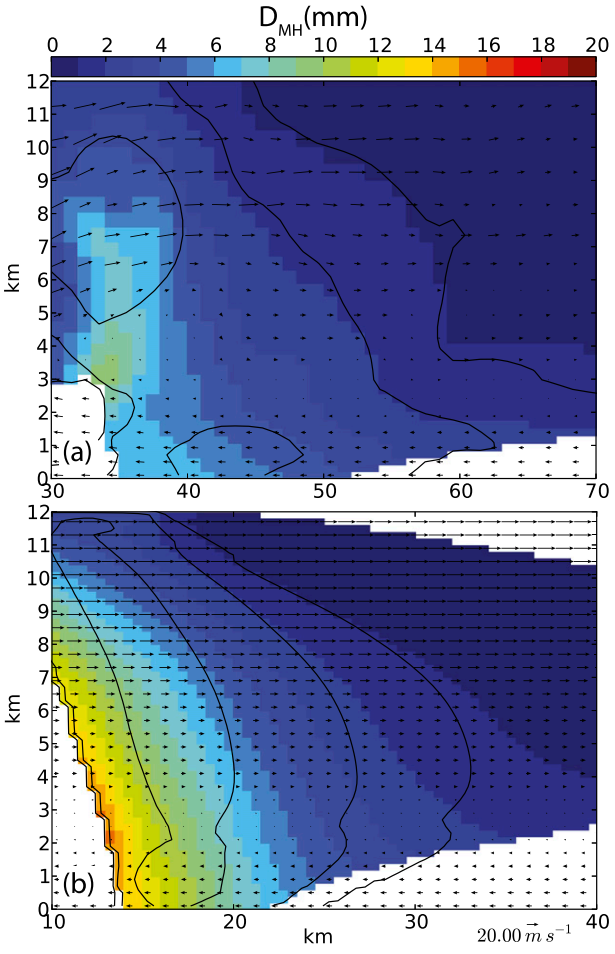

FIG. 16. Vertical cross sections of hail mean volume diameter D_{mh}. (a) SC3R3HVD at location of gray line in Fig. 12h and (b) 3D3R3HVD at location of gray line in Fig. 14h. Black contours are reflectivity with a 20-dBZ increment, starting at 10 dBZ, and storm-relative wind vectors are shown every two grid points.

3) The idealized 3D sedimentation experiments revealed the same trends as the supercell size-sorting simulations. In addition they revealed that the direction of the gradient in mean volume diameter of hail D_{mh} and rain D_{mr} in the precipitation shafts in this study closely aligned with the average storm-relative wind taken over a deep (~0.7–12 km) layer when only hail is allowed to sort. In contrast, when only rain is allowed to sort, the gradient in D_{mr} aligns most closely with the mean storm-relative wind in the shallow submelting (~0.7–3 km) layer, consistent with KR09 (see their Fig. 15). When both hail and rain are allowed to sort, the direction of the D_{mr} gradient is intermediate between the above-mentioned two situations but biased toward the deep-layer storm-relative mean wind. This suggests that a qualitative picture of the near-storm storm-relative wind profile can be achieved by hydrometeor mean diameters estimated from polarimetric variables.
4) The simulated K_{DP} field is qualitatively unaffected by size sorting, consistent with its known sensitivity to the total amount of liquid water present in a radar volume but not as much (relatively speaking) to the PSD or to the presence of hail. In contrast, regions of simulated $\rho_{HV} < 1$ are strongly tied to the presence of graupel or hail mixed with rain. For the bulk of the simulations that predict only one rimed-ice category, the best qualitative agreement with the observations results when the category is more hail like, as was the case with the Z_{DR} field, but the overall predicted magnitudes are too high in the hail-core region. Results are improved when two rimed-ice categories are predicted (graupel/hail and large hail), and the additional predicted hydrometeor diversity drives ρ_{HV} values down to values closer to the observations.
5) The sorting of smaller [O(5–10 mm)] hailstones toward the left flank of the (right moving) supercell and their subsequent melting into large raindrops can produce a secondary region of enhanced Z_{DR} separate from the traditional "Z_{DR} arc." This feature has been tentatively identified in the subject supercell of the current study (the 1 June 2008 storm) and may be present in others as well.

Based on these conclusions, we propose a conceptual model encapsulating the basic physics of the Z_{DR} signatures in the low levels of the forward flank of the 1 June 2008 supercell, which is shown in Fig. 17. Preliminary results from other supercell cases (not shown) are also consistent with this conceptual model, arguing for a more general applicability. The relative degree of size sorting in the hail and rain fields at a given height depends strongly on the wind profile above that height over the depth of the falling precipitation. In addition, the direction of the horizontal gradient in the mean volume diameter of hail and rain at a given height appears to be related to the direction of the storm-relative wind vector averaged over the depth of the precipitation shaft above that height. However, more work needs to be done to quantify these relationships. A similar argument was made regarding the orientation of the Z_{DR} arc in KR09. Thus, the relative location of the largest hail in a supercell and the total amount of sorting may be at least partially determined by the magnitude and direction of the deep-layer storm-relative mean winds. We again note that in some cases, the hail signature in the low levels may be muted or not present (Kumjian and Ryzhkov 2008) because of complete melting of hail.

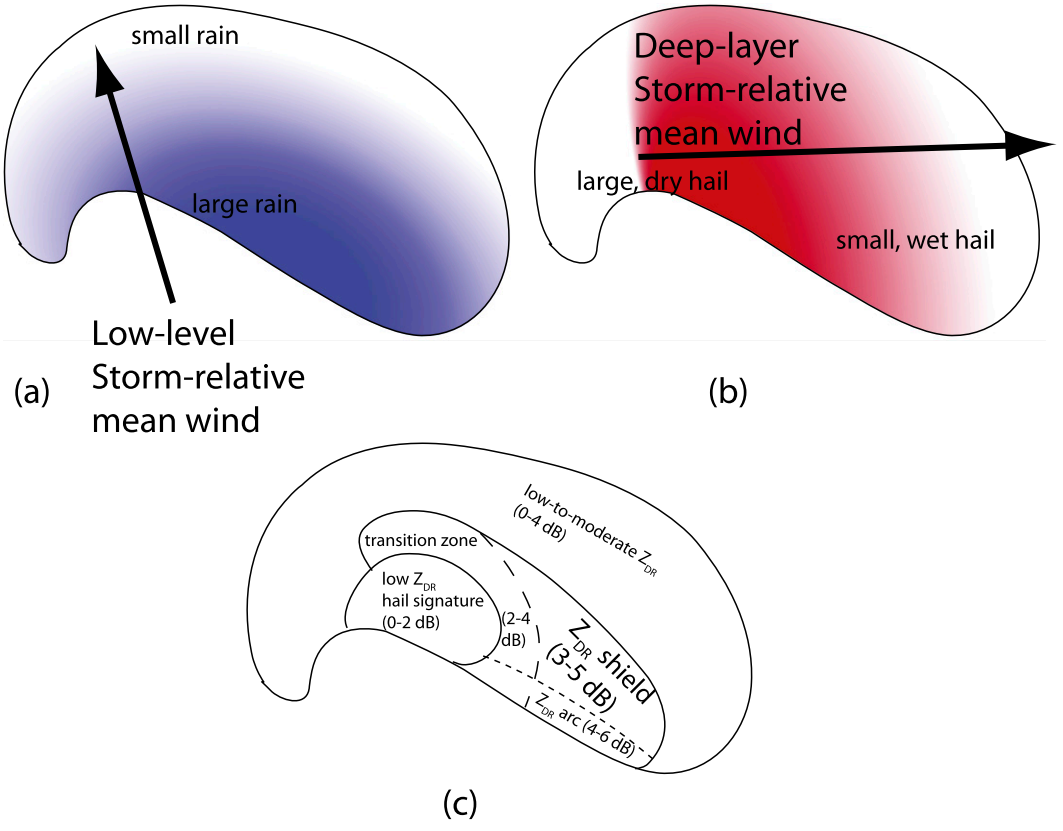

FIG. 17. Schematic summarizing the main conclusions of the study. (a) Gradient of rain mean mass diameter from largest (blue) to smallest (white), along with low-level (~1–3 km) storm-relative mean wind vector; (b) gradient of hail mean mass diameter from largest (red) to smallest (white), along with deep-layer (~1–9 km) storm-relative mean wind vector; and (c) corresponding typical Z_{DR} signatures.

These conclusions on the impact of size sorting on the PSD characteristics of rain and hail would be worth investigating in more detail for more supercell environments, and bin models of melting hail would be particularly useful for evaluating the bulk model results. The study raises other outstanding questions, such as 1) how important are the storm updraft and storm-induced perturbations to the near-storm wind shear (i.e., near the mesocyclone) in affecting the PSD of hail and rain near that feature, as opposed to the preexisting environmental wind shear; 2) can a quantitative relationship between the modeled PSD gradients (such as quantified by the mean volume diameter and shape parameter in the case of the gamma distribution) and the storm-relative environmental winds be found, and how useful might this information be in diagnosing near-storm wind profiles; and 3) how do these size-sorting effects feed back to the overall thermodynamic and dynamic structure of the storm, such as the cold-pool structure and strength, and tornadic activity?

Acknowledgments. This work was primarily supported by the National Research Council and National Science Foundation Postdoctoral Fellowships (Grant AGS-1137702) awarded to the first author, NOAA/National Severe Storms Laboratory, and was partially supported by NOAA/OAR under NOAA–University of Oklahoma Cooperative Agreement NA11OAR4320072, and NSF Grant AGS-1046171. We acknowledge Terry Schuur and other NSSL engineers and scientists who maintain and operate the KOUN polarimetric radar for providing high-quality data. We thank Patrick Marsh for providing portions of the Python code used in the analysis. We thank George Bryan, Hugh Morrison, David Dowell, Glen Romine, Robin Tanamachi, and Jeff Snyder for their helpful comments and discussions on earlier versions of this work and the three anonymous reviewers whose reviews significantly improved the manuscript. The sounding used for the 1 June 2008 supercell environment was derived from an online tool (http://www-angler.larc.nasa.gov/cgi-bin/satimage/sounding.cgi). Graphics were generated using Matplotlib (Hunter 2007).

APPENDIX

Description of Updated Microphysics Scheme

The multimoment microphysics scheme (MZB10) uses a general gamma size distribution (Cohard and Pinty 2000; MY05a; Seifert and Beheng 2006):

$$N_x(D) = N_{Tx}\frac{3\mu_x}{\Gamma(\alpha_x+1)}\lambda_x^{(\alpha_x+1)3\mu_x}D_x^{(\alpha_x+1)3\mu_x-1} \times \exp[-(\lambda_x D_x)^{3\mu_x}], \quad \text{(A1)}$$

where α and μ are the first and second shape parameters, respectively; N_{Tx} is the particle total number concentration; and the slope parameter λ_x can be defined from the zeroth and third moments of the distribution as

$$\lambda_x = \left[\frac{\pi(\alpha_x+1)}{6\upsilon_0}\right]^{1/3} \quad \text{for} \quad \mu_x = 1, \quad \text{(A2)}$$

$$\lambda_x = \left[\frac{\pi(\alpha_x+3)(\alpha_x+2)(\alpha_x+1)}{6\upsilon_0}\right]^{1/3} \quad \text{for} \quad \mu_x = 1/3, \quad \text{(A3)}$$

where υ_0 is the mean particle volume, defined as

$$\upsilon_0 = \frac{\rho_a q_x}{\rho_x N_{Tx}}. \quad \text{(A4)}$$

Microphysical interactions are described by MZB10. The model was updated with the more general warm-rain equations of Cohard and Pinty (2000) to allow a choice for rain to use the original gamma of volume ($\mu_r = 1$) or a gamma of diameter ($\mu_r = 1/3$). The current results use $\mu_r = 1/3$. The calculation of sixth-moment (reflectivity) tendencies follows MY05b, with an addition tendency for graupel/hail and large hail. Graupel/hail and large hail may have predicted mean particle density, which in turn affects the reflectivity moment via the relationship

$$Z_x = \frac{G(\alpha)}{c_x^2}\frac{(\rho_a q_x)^2}{N_{Tx}}, \quad \text{(A5)}$$

where c_x is the coefficient of the mass–diameter relationship $m_x(D) = c_x D^{d_x}$. For graupel/hail and large hail, $d_x = 3$ and $c_x = (\pi/6)\rho_x$. Graupel/hail and large hail use $\mu_x = 1/3$, for which

$$G(\alpha) = \frac{(6+\alpha)(5+\alpha)(4+\alpha)}{(3+\alpha)(2+\alpha)(1+\alpha)}, \quad \text{(A6)}$$

Following MY05b, (A5) can be differentiated with respect to q_x, N_{Tx}, and additionally to c_x for some process A:

$$\left.\frac{dZ_x}{dt}\right|_A = G(\alpha)\rho_a^2\left[2\frac{q_x}{N_{Tx}c_x^2}\left.\frac{dq_x}{dt}\right|_A - \left(\frac{q_x}{N_{Tx}c_x}\right)^2\left.\frac{dN_{Tx}}{dt}\right|_A - 2\frac{q_x^2}{N_{Tx}c_x^3}\left.\frac{dc_x}{dt}\right|_A\right]. \quad \text{(A7)}$$

The microphysical processes actually adjust the particle volume ($V_x = \rho_a q_x/\rho_x$), so rather than adjust Z_x for each process that affects particle density, a net change in density is calculated as

$$\frac{dc_x}{dt} = \frac{\pi}{6}\frac{d\rho_x}{dt} = \frac{\pi}{6}\frac{\rho_x(t_0+\Delta t)-\rho_x(t_0)}{\Delta t}, \quad \text{(A8)}$$

$$\rho_x(t_0) = \frac{\rho_a q_x(t_0)}{V_x(t_0)}, \quad \text{(A9)}$$

$$\rho_x(t_0+\Delta t) = \frac{\rho_a[q_x(t_0)+\Delta q]}{[V_x(t_0)+\Delta V]}, \quad \text{(A10)}$$

where Δq and ΔV are the net changes to mass mixing ratio and particle volume, respectively (Mansell and Ziegler 2013). The density ρ_x is limited within the allowed range from $\rho_{x,\min}$ to $\rho_{x,\max}$ for the particle type.

REFERENCES

Balakrishnan, N., and D. S. Zrnić, 1990: Use of polarization to characterize precipitation and discriminate large hail. *J. Atmos. Sci.,* **47,** 1525–1540.

Borowska, L., A. Ryzhkov, D. S. Zrnić, C. Simmer, and R. Palmer, 2011: Attenuation and differential attenuation of 5-cm-wavelength radiation in melting hail. *J. Appl. Meteor. Climatol.,* **50,** 59–76.

Bringi, V. N., and V. Chandrasekar, 2001: *Polarimetric Doppler Weather Radar.* Cambridge, 636 pp.

——, T. Tang, and V. Chandrasekar, 2004: Evaluation of a new polarimetrically based *Z–R* relation. *J. Atmos. Oceanic Technol.,* **21,** 612–623.

Cohard, J.-M., and J.-P. Pinty, 2000: A comprehensive two-moment warm microphysical bulk scheme. I: Description and tests. *Quart. J. Roy. Meteor. Soc.,* **126,** 1815–1842.

Coniglio, M. C., D. J. Stensrud, and L. J. Wicker, 2006: Effects of upper-level shear on the structure and maintenance of strong quasi-linear mesoscale convective systems. *J. Atmos. Sci.,* **63,** 1231–1252.

Dawson, D. T., M. Xue, J. A. Milbrandt, and M. K. Yau, 2010: Comparison of evaporation and cold pool development between single-moment and multimoment bulk microphysics schemes in idealized simulations of tornadic thunderstorms. *Mon. Wea. Rev.,* **138,** 1152–1171.

Ferrier, B. S., 1994: A double-moment multiple-phase four-class bulk ice scheme. Part I: Description. *J. Atmos. Sci.,* **51,** 249–280.

Giangrande, S. E., and A. V. Ryzhkov, 2008: Estimation of rainfall based on the results of polarimetric echo classification. *J. Appl. Meteor. Climatol.,* **47,** 2445–2462.

Gilmore, M. S., J. M. Straka, and E. N. Rasmussen, 2004: Precipitation uncertainty due to variations in precipitation particle parameters within a simple microphysics scheme. *Mon. Wea. Rev.,* **132,** 2610–2627.

Gourley, J. J., P. Tabary, and J. Parent du Chatelet, 2007: A fuzzy logic algorithm for the separation of precipitating from nonprecipitating echoes using polarimetric radar observations. *J. Atmos. Oceanic Technol.,* **24,** 1439–1451.

Heinselman, P. L., and A. V. Ryzhkov, 2006: Validation of polarimetric hail detection. *Wea. Forecasting,* **21,** 839–850.

Herzegh, P. H., and A. R. Jameson, 1992: Observing precipitation through dual-polarization radar measurements. *Bull. Amer. Meteor. Soc.,* **73,** 1365–1374.

Hunter, J. D., 2007: Matplotlib: A 2D graphics environment. *Comput. Sci. Eng.,* **9,** 90–95.

Jung, Y., G. Zhang, and M. Xue, 2008: Assimilation of simulated polarimetric radar data for a convective storm using the ensemble Kalman filter. Part I: Observation operators for reflectivity and polarimetric variables. *Mon. Wea. Rev.,* **136,** 2228–2245.

——, M. Xue, and G. Zhang, 2010: Simulations of polarimetric radar signatures of a supercell storm using a two-moment bulk microphysics scheme. *J. Appl. Meteor. Climatol.,* **49,** 146–163.

Kumjian, M. R., and A. V. Ryzhkov, 2008: Polarimetric signatures in supercell thunderstorms. *J. Appl. Meteor. Climatol.,* **47,** 1940–1961.

——, and ——, 2009: Storm-relative helicity revealed from polarimetric radar measurements. *J. Atmos. Sci.,* **66,** 667–685.

——, and ——, 2012: The impact of size sorting on the polarimetric radar variables. *J. Atmos. Sci.,* **69,** 2042–2060.

——, ——, V. M. Melnikov, and T. J. Schuur, 2010: Rapid-scan super-resolution observations of a cyclic supercell with a dual-polarization WSR-88D. *Mon. Wea. Rev.,* **138,** 3762–3786.

Mansell, E. R., 2010: On sedimentation and advection in multi-moment bulk microphysics. *J. Atmos. Sci.,* **67,** 3084–3094.

——, and C. L. Ziegler, 2013: Aerosol effects on simulated storm electrification and precipitation in a two-moment bulk microphysics model. *J. Atmos. Sci.,* **70,** 2032–2050.

——, ——, and E. C. Bruning, 2010: Simulated electrification of a small thunderstorm with two-moment bulk microphysics. *J. Atmos. Sci.,* **67,** 171–194.

Milbrandt, J. A., and M. K. Yau, 2005a: A multimoment bulk microphysics parameterization. Part I: Analysis of the role of the spectral shape parameter. *J. Atmos. Sci.,* **62,** 3051–3064.

——, and ——, 2005b: A multimoment bulk microphysics parameterization. Part II: A proposed three-moment closure and scheme description. *J. Atmos. Sci.,* **62,** 3065–3081.

——, and R. McTaggart-Cowan, 2010: Sedimentation-induced errors in bulk microphysics schemes. *J. Atmos. Sci.,* **67,** 3931–3948.

——, and H. Morrison, 2013: Prediction of graupel density in a bulk microphysics scheme. *J. Atmos. Sci.,* **70,** 410–429.

Mishchenko, M. I., 2000: Calculation of the amplitude matrix for a nonspherical particle in a fixed orientation. *Appl. Opt.,* **39,** 1026–1031.

Naylor, J., and M. S. Gilmore, 2012: Convective initiation in an idealized cloud model using an updraft nudging technique. *Mon. Wea. Rev.,* **140,** 3699–3705.

Park, H. S., A. V. Ryzhkov, D. S. Zrnić, and K.-E. Kim, 2009: The hydrometeor classification algorithm for the polarimetric WSR-88D: Description and application to an MCS. *Wea. Forecasting,* **24,** 730–748.

Rasmussen, R. M., and A. J. Heymsfield, 1987: Melting and shedding of graupel and hail. Part I: Model physics. *J. Atmos. Sci.,* **44,** 2754–2763.

——, V. Levizzani, and H. R. Pruppacher, 1984: A wind tunnel and theoretical study on the melting behavior of atmospheric ice particles: III. Experiment and theory for spherical ice particles of radius $> 500\ \mu$m. *J. Atmos. Sci.,* **41,** 381–388.

Romine, G. S., D. W. Burgess, and R. B. Wilhelmson, 2008: A dual-polarization-radar-based assessment of the 8 May 2003 Oklahoma City area tornadic supercell. *Mon. Wea. Rev.,* **136,** 2849–2870.

Ryzhkov, A. V., and D. S. Zrnić, 1998: Discrimination between rain and snow with a polarimetric radar. *J. Appl. Meteor.,* **37,** 1228–1240.

——, T. J. Schuur, D. W. Burgess, P. L. Heinselman, S. E. Giangrande, and D. S. Zrnić, 2005a: The Joint Polarization Experiment: Polarimetric rainfall measurements and hydrometeor classification. *Bull. Amer. Meteor. Soc.,* **86,** 809–824.

——, ——, ——, and D. S. Zrnić, 2005b: Polarimetric tornado detection. *J. Appl. Meteor.,* **44,** 557–570.

Ryzhkov, A., M. Pinsky, A. Pokrovsky, and A. Khain, 2011: Polarimetric radar observation operator for a cloud model with spectral microphysics. *J. Appl. Meteor. Climatol.,* **50,** 873–894.

Seifert, A., and K. D. Beheng, 2006: A two-moment cloud microphysics parameterization for mixed-phase clouds. Part 1: Model description. *Meteor. Atmos. Phys.,* **92,** 45–66.

Seliga, T. A., and V. N. Bringi, 1976: Potential use of radar differential reflectivity measurements at orthogonal polarizations for measuring precipitation. *J. Appl. Meteor.,* **15,** 59–76.

Srivastava, R. C., 1978: Parameterization of raindrop size distributions. *J. Atmos. Sci.,* **35,** 108–117.

Straka, J. M., D. S. Zrnić, and A. V. Ryzhkov, 2000: Bulk hydrometeor classification and quantification using polarimetric radar data: Synthesis of relations. *J. Appl. Meteor.,* **39,** 1341–1372.

Tessendorf, S. A., L. J. Miller, K. C. Wiens, and S. A. Rutledge, 2005: The 29 June 2000 supercell observed during STEPS. Part I: Kinematics and microphysics. *J. Atmos. Sci.,* **62,** 4127–4150.

Vivekanandan, J., W. M. Adams, and V. N. Bringi, 1991: Rigorous approach to polarimetric radar modeling of hydrometeor orientation distributions. *J. Appl. Meteor.,* **30,** 1053–1063.

Wacker, U., and A. Seifert, 2001: Evolution of rain water profiles resulting from pure sedimentation: Spectral vs. parameterized description. *Atmos. Res.,* **58,** 19–39.

Waterman, P. C., 1969: Scattering by dielectric obstacles. *Alta Freq.,* **38,** 348–352.

Wicker, L. J., and R. B. Wilhelmson, 1995: Simulation and analysis of tornado development and decay within a three-dimensional supercell thunderstorm. *J. Atmos. Sci.,* **52,** 2675–2703.

Wisner, C., H. D. Orville, and C. Myers, 1972: A numerical model of a hail-bearing cloud. *J. Atmos. Sci.,* **29,** 1160–1181.

Yussouf, N., E. R. Mansell, L. J. Wicker, D. M. Wheatley, and D. J. Stensrud, 2013: The ensemble Kalman filter analyses and forecasts of the 8 May 2003 Oklahoma City tornadic supercell storm using single and double moment microphysics schemes. *Mon. Wea. Rev.,* **141,** 3388–3412.

Ziegler, C. L., 1985: Retrieval of thermal and microphysical variables in observed convective storms. Part I: Model development and preliminary testing. *J. Atmos. Sci.,* **42,** 1487–1509.

Zrnić, D. S., and A. V. Ryzhkov, 1999: Polarimetry for weather surveillance radars. *Bull. Amer. Meteor. Soc.,* **80,** 389–406.

——, A. Ryzhkov, J. Straka, Y. Liu, and J. Vivekanandan, 2001: Testing a procedure for automatic classification of hydrometeor types. *J. Atmos. Oceanic Technol.,* **18,** 892–913.